

1 Wet-Radome Attenuation in ARM Cloud Radars and Its Utilization in Radar Calibration Using Disdrometer
2 Measurements

3
4 Min Deng¹, Scott E. Giangrande¹, Michael P. Jensen¹, Karen Johnson¹, Christopher R. Williams²,
5 Jennifer M. Comstock³, Ya-Chien Feng³, Alyssa Matthews³, Iosif A. Lindenmaier³, Timothy G.
6 Wendler³, Marquette Rocque³, Aifang Zhou¹, Zeen Zhu¹, Edward Luke¹, and Die Wang¹

7
8
9 ¹ Brookhaven National Laboratory, Environmental and Climate Sciences Department, Upton,
10 New York

11 ² University of Colorado Boulder, Colorado Center for Astrodynamics Research, Boulder,
12 Colorado

13 ³ Pacific Northwest National Laboratory, Richland, Washington

14
15
16 *Correspondence to:* Min Deng (mdeng@bnl.gov)

17
18
19 Manuscript to be submitted to AMT publication.

20
21
22
23
24
25
26
27
28
29
30
31
32
33
34

35 Abstract

36

37 A relative calibration technique has been developed for the U.S. Department of Energy's
38 (DOE) Atmospheric Radiation Measurement (ARM) user facility Ka-Band ARM Zenith Radars
39 (KAZRs). This method uses the signal attenuation caused by water on the radome to estimate
40 reflectivity factor (Z_e) offsets. The wet-radome attenuation (WRA) is assumed to follow a log-
41 linear relationship with rainfall rate during light and moderate rain, as measured by a collocated
42 surface disdrometer. The technique has an uncertainty of approximately 3 dB, due to factors such
43 as disdrometer measurement error, rain variability between radar and disdrometer sample volumes,
44 and the fitting function's uncertainty for the WRA behavior. A practical advantage of this WRA-
45 based approach to shorter-wavelength radar monitoring is that, while it requires a reference
46 disdrometer, it proves feasible for a wider range of collocated disdrometer measurements
47 compared to traditional direct disdrometer comparison at the onset of light rain. This technique
48 thus offers a cost-effective monitoring tool for remote or long-term radar deployments.

49 This calibration technique was applied during the ARM TRacking Aerosol Convection
50 interactions ExpeRiment (TRACER) from October 2021 through September 2022. The estimated
51 Z_e offsets were compared against traditional radar calibration and monitoring methods using
52 available datasets from this campaign. Results show that the WRA-based offsets align closely with
53 mean offsets found between cloud radars and from direct disdrometer comparison near the onset
54 of rain, while also reflecting similar offset and campaign-long trends when compared to collocated,
55 independently calibrated radar wind profiler. Nevertheless, overall, the KAZR Z_e offsets estimated
56 during TRACER remained stable at approximately 2 dBZ lower than the disdrometer estimates
57 from the campaign start until the end of June 2022, afterward, the offsets increased to around 7
58 dBZ by the campaign's end. This increase is linked to a drop of about 1 dB in transmitter power
59 toward the end of the project.

60

61

62

63

64

65 Short Summary

66

67 A relative calibration technique is developed for the cloud radar by monitoring the intercept
68 of the wet-radome attenuation (WRA) log-linear behavior as a function of rainfall rates in light
69 and moderate rain conditions. This WRA technique is applied to the measurements during the
70 ARM TRACER campaign and reports Z_e offsets that compare favorably with the traditional
71 disdrometer comparison near the time of rain onset, while also demonstrates similar offset and
72 campaign-long trends with respect to collocated and independently calibrated reference radars.

73

74

75

76

77 1 Introduction

78 The U.S. Department of Energy (DOE) Atmospheric Radiation Measurement (ARM) user
79 facility operates millimeter-wavelength cloud radars (35 and 94 GHz) at various global fixed and
80 mobile sites (e.g., Mather and Voyles, 2013; Miller et al., 2016; Kollias et al., 2007, 2020). These
81 "cloud" radars are often more sensitive than traditional centimeter-wavelength weather radars,
82 allowing them to detect cloud droplets more effectively. However, this sensitivity comes with a
83 trade-off, as shorter wavelengths are prone to partial or complete attenuation in clouds and
84 precipitation. Such attenuation introduces uncertainties in key radar-derived properties like
85 reflectivity factor (Z_e), affecting cloud and hydrological retrieval accuracy (e.g., Matrosov, 2005;
86 Deng et al., 2014; Zhu et al., 2019).

87 Given the importance of accurate Z_e measurements, the routine deployment and operation
88 of cloud radars necessitate frequent calibration and monitoring activities. In general, more rigorous
89 radar calibration efforts can be implemented (e.g., Russchenberg et al., 2020), but these approaches
90 are often system-specific and require highly skilled engineers or technicians, significant time, and
91 specialized equipment (within ARM, e.g., Mead, 2010). For weather and climate applications,
92 radar-based research has increasingly turned to "relative" calibration techniques, which rely on Z_e
93 estimates from nearby reference instruments or expectations based on intrinsic properties of the
94 hydrometeors or other media (e.g., Bringi and Chandrasekar, 2001; Giangrande et al., 2005; Protat

95 et al., 2011; Kollias et al., 2019; Maahn et al., 2019; Williams et al., 2023). Several of these
96 “natural” calibration concepts have proven effective for quantifying radar performance in many
97 hydrological applications requiring Ze estimates within 2-3 dBZ. The simplest approach is often a
98 cross-comparison of Ze characteristics with collocated, calibrated reference radars. For example,
99 extended comparisons of clouds near ARM ground sites using CloudSat radar measurements have
100 successfully monitored the long-term ARM cloud radar record (Protat et al., 2011; Kollias et al.,
101 2019). For finer-scale comparisons during ARM deployments, the Ka-Band ARM Zenith Radar
102 (KAZR) is often collocated with a Radar Wind Profiler (RWP, 915 or 1290 MHz) and the Ka- and
103 X-band Scanning ARM Cloud Radar (KaSACR/ XSACR), which are easier to monitor using
104 independent techniques better suited to scanning and/or longer-wavelength radar.

105 Among the various methods of relative cloud radar monitoring, a common approach relies
106 on surface disdrometer observations. The reflectivity factor can be estimated for assumed rain
107 properties using techniques such as T-matrix scattering algorithms applied to the drop size
108 distribution of rain measured by the surface disdrometer (Mishchenko et al., 1996). Comparing
109 radar-measured reflectivity near the surface with disdrometer-estimated reflectivity provides a
110 common way to estimate radar calibration offsets (e.g., Kollias et al., 2019; Myagkov et al., 2020;
111 Russchenberg et al., 2020; and Lamer et al., 2021). Disdrometer comparison techniques like this
112 have been implemented as routine procedures for radar monitoring, such as in the Aerosol Cloud
113 Tracer Gas Research Infrastructure (ACTRIS) network in Europe (Dupont et al., 2022). For radars
114 that experience negligible attenuation in rain, such procedures are often straightforward to
115 implement across a variety of widespread precipitating conditions (e.g., Williams et al., 2023).
116 However, for shorter radar wavelengths, where gaseous attenuation, rain attenuation, and wet-
117 radome attenuation are not negligible, applying this approach can be more complicated.

118 Specifically, the two-way attenuation associated with radome wetting (referred to here as
119 wet radome attenuation or WRA) is a well-known phenomenon. During rainfall, water droplets
120 bead on the surface of the radar radome, forming a wet film that eventually flows off the radome
121 once it reaches sufficient mass, similar to the water layer on a car window. Droplets impacting the
122 radome during persistent rain further alter the water depth through bouncing and splashing (Gibble,
123 1964; Anderson, 1975; Yu et al., 2021). For long-wavelength radars, WRA is often considered
124 negligible (Thompson et al., 2012; Kurri and Huuskonen, 2008). However, for shorter-wavelength
125 radars, the impact of WRA is potentially more significant. For example, at X-band, Bechini et al.

126 (2010) and Gorgucci et al. (2013) observed a loss of 5 dB in moderate rain by comparing
127 simultaneous X-band radar measurements at close range with a collocated video disdrometer. This
128 WRA has been shown to depend on the thickness of the water film (d) on the radome, which in
129 turn is a function of rain rate, as described by the Gibble formula (Gibble, 1964; Anderson, 1975):

130
$$d = \left(\frac{3\mu_k r R}{2g} \right)^{1/3}, \quad (1)$$

131 where μ_k is the kinematic viscosity of water (that also varies with temperature), r is the radome
132 radius, R is the rain rate, and g is the gravitational acceleration. Additional relations between WRA
133 and R have been developed based on the Gibble's $R^{1/3}$ formula by Frasier et al. (2013) and
134 Gorgucci et al. (2013) for X-band radar calibration studies.

135 Few studies have considered WRA for assessing cloud radar offsets at Ka-band (35 GHz).
136 As the water absorption coefficient is inversely proportional to wavelength (Bertie et al. 1996,
137 Segelstein 1981), the WRA at Ka-band is approximately as three times as that at X-band for the
138 same depth of rainwater on the radome. It is understood that WRA will impact direct estimates of
139 the offset between cloud radar and disdrometer Z_e estimates in rainy conditions, and faulty offset
140 assessment after rain ends may occur owing to extended radome drying delays. Therefore, direct
141 comparison concepts previously cited typically consider only the periphery cloud, drizzle or light
142 rain conditions (i.e., $R < 1\text{-}2 \text{ mm hr}^{-1}$) at the onset of a rainfall event to minimize various forms of
143 attenuation. This often is a very stringent and subjective employment of these conditions: First, it
144 limits the opportunities for direct disdrometer monitoring of cloud radar to a selected window of
145 rainfall rates and event timing. Identifying these light rain or drizzling conditions is also contingent
146 on the requirements for collecting high-quality disdrometer measurements (i.e., those that require
147 significant droplet number counts), wherein a separate rain rate cut-off may be required to avoid
148 significant WRA. Overall, it is potentially useful to establish other forms of cloud radar monitoring
149 that could benefit from a wider range of observations collected during precipitation window.

150 In this study, we first identify intervals of WRA for Ka-band radars by comparing
151 observations from ARM's KAZR with a collocated suite of instruments, including a surface
152 disdrometer, a calibrated RWP, and KaSACR/XSACR observations collected in vertical pointing
153 (VPT) modes during the Tracking Aerosol Convection Interactions Experiment (TRACER). We
154 then develop a new WRA fitting technique and apply it to calibrate the Z_e offset for KAZR using

155 TRACER measurements. The performance of this technique is evaluated against three traditional
156 relative calibration or monitoring methods for Ka-band radar: (i) direct disdrometer comparisons
157 of Ze in light rain at the onset of rain events, (ii) a cross-comparison with independently calibrated
158 RWP measurements, and (iii) a cross-comparison with collocated scanning KaSACR
159 measurements.

160 The paper is organized as follows. Section 2 introduces the radar datasets and supporting
161 TRACER datasets used in this study. In Section 3, a relative calibration technique is developed
162 with daily KAZR and KaSACR measurements collected during light and moderate rainfall
163 conditions. In Section 4, the technique is applied to the KAZR measurements during the TRACER
164 campaign to assess the long-term calibration offset trend for KAZR, and the result is evaluated
165 against other calibration methods. A summary of the performance of this WRA technique for
166 relative offset monitoring is provided in Section 5.

167

168 2 TRACER Dataset Description and Comparisons

169 The TRACER campaign took place in the Houston, TX region from 1 October 2021 to 30
170 September 2022 (Jensen et al., 2019, 2022, and 2023) with a goal of studying the interactions of
171 aerosols and convective clouds. The main surface measurement site was located at La Porte, TX
172 housed the deployment of the first ARM Mobile Facility (AMF1; Miller et al., 2016). The AMF1
173 consists of several ground-based remote-sensing and profiling instruments, and included the
174 deployment of the KAZR, KaSACR/XSACR, and radar wind profiler (RWP) units that serve as
175 the radars for this study. The surface instrumentation also included multiple laser and video
176 disdrometers as reference anchors.

177

178 2.1 TRACER Cloud Radars (KAZR and KaSACR/XSACR)

179 The KAZR (Widener et al., 2012) is a successor to ARM's highly successful millimeter-
180 wavelength cloud radar (MMCR). The KAZR has a flat radome inclined at 4°. A complete list of
181 KAZR specifications is provided in Table 1. The KAZR transmits and receives two types of pulses:
182 (i) the burst pulse, a simple narrow pulse of radio-frequency energy (referred to as "GE" mode),
183 and (ii) the chirp pulse, a longer, frequency-modulated pulse with higher transmitted energy and
184 greater sensitivity, but with data collection starting at a higher range due to the larger blind zone
185 imposed by the longer pulse length (referred to as "MD" mode). Although the MD mode is more

186 sensitive to clouds (i.e., has a lower minimum detectable Z_e), only the KAZR GE mode data are
187 used for disdrometer comparisons, as near-surface observations are required.

188 The KaSACR and XSACR are co-mounted on a scanning pedestal (Kollias et al., 2014a,
189 2014b). During TRACER, the KaSACR/XSACR typically followed a 10-minute scanning pattern:
190 (i) two low-level plan position indicator (PPI) scans at 1° and 2° elevation, followed by (ii) 6
191 hemispheric range height indicator (HSRHI) scans at 30° azimuth intervals, and then (iii) 2 minutes
192 of vertical pointing (VPT) mode. This study utilizes the 2-minute VPT mode segment from each
193 10-minute scanning sequence (i.e., nominal scanning VPT mode). The specifications during VPT
194 mode are listed in Table 1. For one event on September 3-4, 2022, the KaSACR/XSACR was
195 temporarily operated exclusively in VPT mode (i.e., stationary VPT mode) for radar cross-
196 calibration purposes. The KaSACR has an inclined radome similar to the KAZR but is relatively
197 newer, with potentially less deterioration of its hydrophobic coating. The XSACR has a conical
198 radome with a slant angle of 45° to the surface. Overall, the WRA effect is expected to be smaller
199 for the XSACR compared to either Ka-band radar, due to wavelength-dependent differences as
200 well as the improved radome design. The KaSACR calibration offsets between May and
201 September 2022 are expected to be stable based on ground clutter analysis using relative
202 calibration adjustment (RCA) techniques (Skolnik, 2000; Hunzinger et al., 2020) and are reported
203 to be close to 0 dB, according to the ARM TRACER radar b1 data processing report (Feng et al.,
204 2024).

205 To compare with Z_e estimates from disdrometer measurement, radar measurements at 500
206 m are selected and corrected for gaseous attenuation using nearby radiosonde measurements (e.g.,
207 Ulaby et al., 1981). Rain attenuation is also corrected using specific attenuation coefficient (K)
208 estimates from disdrometer measurement, assuming a uniform layer between the surface and 500
209 m. There is concern that the radar might saturate, particularly for the KaSACR near its minimum
210 range, which could introduce a low bias in measured Z_e compared to disdrometer Z_e . Based on
211 communication with an ARM radar engineer, the power associated with the highest voltage
212 digitizable by the radar's Analog-to-Digital Converter (ADC) is 5.9 dBm. The corresponding
213 KAZR saturation reflectivity at 500 meters is approximately 45 dBZ, given its calibration constant
214 of -12 dBm. Similarly, the KaSACR saturation reflectivity at 500 m is about 31 dBZ, given its
215 calibration constant of -26 dBm. The measured radar reflectivities from both KAZR and KaSACR

216 at 500 m are generally less than 25 dBZ, well below the saturation threshold. Additional supporting
217 evidence through radar profile comparisons can be found in the supplementary material.

218

219 2.2 Surface Disdrometer Measurements and Value-Added Products

220 A Parsivel2 laser disdrometer (LDIS) and a two-dimensional video disdrometer (VDIS)
221 unit were deployed at the main site during TRACER in very close proximity to the cloud radars.
222 For disdrometer geophysical quantities and data quality control, procedures follow the standard
223 drop size distribution (DSD) filtering in Giangrande et al. (2019) implemented by ARM in their
224 precipitation value-added products (Video Disdrometer Quantities--VDISQUANTS and Laser
225 Disdrometer Quantities--LDQUANTS, Hardin et al., 2020). These products employ several fall
226 speed checks, temperature, drop shape/canting assumptions, larger drop restrictions (no drop sizes
227 > 5 mm) and drop count thresholds (> 20 drops per minute for a valid DSD) that impact estimates
228 of hydrometeor Z_e and K for radar frequencies using a T-matrix scattering algorithm (Mishchenko
229 et al., 1996). As further discussed within the disdrometer literature (Tokay et al., 2001, 2013;
230 Giangrande et al., 2019; Wang et al., 2021), the VDIS is considered the more reliable and sensitive
231 disdrometer to a wider range of drop sizes under nominal light rain operating conditions.
232 Therefore, the estimated Z_e at Ka-band in VDISQUANTS is used within this study as our ground
233 truth for KAZR calibration and surface rain rate, while the LDIS products have been used as an
234 independent reference for monitoring RWP Z_e estimates (e.g., Williams et al., 2023), which is
235 required for additional direct radar comparisons in Section 4.

236

237 2.3 Radar Wind Profiler (RWP)

238 The RWP deployed during TRACER was operated using an adaptive scanning mode,
239 switching between a traditional boundary layer horizontal wind mode and a vertically pointing
240 precipitation mode adopted by ARM for its recent deep convective cloud campaigns (e.g., Tridon
241 et al., 2013; Giangrande et al., 2013, 2016). When the signal-to-noise ratio in the vertical beam
242 exceeded a predefined threshold, the RWP switched into this precipitation mode and employs a
243 single vertically pointing beam operation. This mode transmitted short- and long-pulses to observe
244 echoes close to the radar with fine resolution, or further from the radar with coarser
245 resolution. Important to this study, the TRACER RWP mode switching sometimes prevented the
246 RWP from immediately observing the periphery lightly precipitating clouds as they passed over

247 the AMF1 site. However, this mode-switching sampling issue does not impact the bulk KAZR-
248 RWP Ze cross-comparisons because we primarily consider daily average behaviors. As before, the
249 RWP Ze measurements in precipitation mode were calibrated independently using collocated
250 LDIS observations (i.e., Williams et al., 2023), who found a standard deviation of 2 - 4 dBZ
251 between the RWP at 500 m and LDIS.

252 253 3 Cloud Radar Ze Calibration and Monitoring: Development of a New WRA Technique

254 255 3.1 Identification of WRA: KaSACR/XSACR in Stationary VPT Modes

256
257 Figure 1a-c show the measured reflectivity (Ze) from the KaSACR/XSACR and the KAZR
258 GE mode on 03-04 September 2022, when the KaSACR/XSACR was operated exclusively in a
259 stationary vertically pointing (VPT) mode. Two intervals of widespread rainfall were captured: the
260 first around 17-19 UTC and the second from 20–02 UTC. A radar "bright band" signature,
261 indicative of the melting level, appears around 5 km AGL during this event. After 02 UTC (20
262 LT), light rain gave way to high, scattered clouds through the night, until thick anvil clouds from
263 nearby convection moved in around 15 UTC (09 LT). Overall, the KaSACR/XSACR reported
264 similar Ze values under peripheral cloudy conditions and during light rain, where rain attenuation
265 and WRA were minimal. As expected, larger discrepancies between XSACR and KaSACR (with
266 the KaSACR showing lower, attenuated Ze values) occurred during heavier rainfall from 22-00
267 UTC. The KAZR consistently reported lower Ze values than the KaSACR, with differences often
268 exceeding 5 dBZ throughout the event.

269 The Ze difference between the KaSACR and KAZR values in Fig.1d exhibits strong
270 temporal variation but limited vertical variation, indicating that the difference is likely driven by
271 the radar or its local environment (e.g., WRA) rather than atmospheric features. The minimum
272 difference of ~7 dB in high clouds, observed around 17-18 UTC and again the next morning (15-
273 17 UTC on 4 September), suggests an overall Ze offset between the KAZR and KaSACR. A
274 minimum difference of ~7 dB in rain (at 19, 21, and 23 UTC) indicates similar WRA behavior for
275 both KAZR and KaSACR. However, a prolonged increase in this difference after moderate rain,
276 especially under humid conditions at night (0-12 UTC, or 18-6 LT), suggests that the KAZR and
277 KaSACR may experience additional discrepancies after rain or in high humidity, possibly due to
278 the older, less hydrophobic radome of the KAZR, as noted in the Cloud, Aerosol, and Complex

279 Terrain Interactions (CACTI) campaign (Varble et al. 2021; Hardin et al. 2020). Accurate
280 correction for KAZR wet-radome attenuation is challenging and beyond the scope of this study;
281 however, WRA behavior in rain can provide a basis for tracking KAZR calibration, as will be
282 demonstrated in the following sections.

283 The time series of rain rate (R), K and Z_e estimates at Ka- and X-bands from
284 VDISQUANTS for the 03-04 September 2022 case are shown in Fig. 2a and b. The sampled R
285 from the disdrometer is commonly less than 1 mm hr^{-1} , but approach 5 mm hr^{-1} around 2330 UTC.
286 The Z_e from KAZR, KaSACR/ XSACR at 500 m are plotted in Fig. 2b. For all collocated
287 precipitating samples, the XSACR Z_e (black crosses) has a high correlation with estimated Z_e (r
288 = 0.95), while KAZR Z_e (blue crosses) are biased low when directly compared to the disdrometer
289 Z_e , which is exacerbated further in heavy rain contexts. KaSACR Z_e (red cross) falls in between
290 XSACR and KAZR Z_e values.

291 Figure 2c shows the differences between measured and estimated Z_e (Dze) for KAZR,
292 KaSACR, and XSACR. The XSACR exhibits a minimum Dze of 0 dB when the rain rate is below
293 0.1 mm hr^{-1} , but this difference can reach 5 dB around 23:30 UTC. The KaSACR Dze is
294 approximately 1 dB at 18 and 21 UTC, while the KAZR Dze is around 7 dB, suggesting calibration
295 offsets of around 1 dB for KaSACR and 7 dB for KAZR. Both KaSACR and KAZR Z_e are further
296 biased lower by an additional 13 dBZ when the rain rate reaches approximately 5 mm hr^{-1} around
297 23:30 UTC. This 13 dB reduction in KAZR and KaSACR estimates is significantly larger than the
298 expected two-way attenuation in rain at Ka-band ($\sim 2 \text{ dB}$, Figure 2a), suggesting that other factors,
299 such as WRA, contribute increasingly to the observed offset in rain. Additionally, WRA for both
300 KAZR and KaSACR likely shows similar dependence on rain rates.

301 The estimated Z_e from VDISQUANTS during the entire TRACER campaign are plotted
302 as a function of R in Fig. 3. The estimated Z_e for both X- and Ka-bands exhibits a log-linear
303 relationship with R . When R exceeds 2 mm hr^{-1} , the Z_e values begin to diverge, and the difference
304 between the two wavelengths increases as R rises, likely due to resonance effects associated with
305 non-Rayleigh scattering (Baldini et al., 2012). The cumulative probability distribution (CDF) of
306 rain rates (red line in Figure 3) shows that about 15% of disdrometer samples have $R < 0.1 \text{ mm}$
307 hr^{-1} , indicating limited data for traditional direct disdrometer comparison at precipitation onset.
308 However, approximately 85% of TRACER data samples have $R < 5 \text{ mm hr}^{-1}$, suggesting that this

309 large range of data sample is suitable for the WRA technique applications discussed in the
310 following sections.

311 3.2 Identification of WRA: KaSACR/XSACR in its Scanning-VPT Mode

312
313 To further illustrate the WRA, we compared radar and disdrometer measurements while
314 the KaSACR/XSACR operated in its nominal 10-minute scanning sequence during a stratiform
315 rain event observed on 11 August 2022, between 01-04 UTC (Fig. 4). The radars were exposed to
316 persistent rainfall, ranging from 1 mm hr⁻¹ at 01 UTC to over 5 mm hr⁻¹ around 02:15 UTC, leading
317 to strong radar signal attenuation, particularly visible in the KAZR Ze vertical gradient above 4
318 km (Fig. 4a). After 03 UTC, the surface rain intensity was so low that the disdrometer could not
319 effectively measure rain drop size distributions (DSDs) for Ze estimates due to insufficient drop
320 counts (<20 drops/minute) (Fig. 4b).

321 The disdrometer-estimated surface Ze at Ka- (black diamonds) and X-bands (blue
322 diamonds) in Fig. 4c consistently show values close to 30 dBZ when rain rates are near 1 mm hr⁻¹,
323 while the KAZR Ze is around 15 dBZ, resulting in a Dze of 15 dB against the disdrometer, as
324 shown in Fig. 4d. During this event, there is an 8-minute gap in every 2 minutes of VPT
325 measurements due to the PPI and HSRHI scans. The collocation of the 2-minute VPT data is
326 extended to a 6-minute window by averaging KaSACR/XSACR and VDISQUANTS data over a
327 ±2-minute interval.

328 The KaSACR Ze values (red crosses) in Fig. 4c display a sawtooth pattern within each 10-
329 minute scanning cycle. Each cycle begins with Ze values close to the XSACR Ze, followed by a
330 decline towards the KAZR Ze value as time progresses, with the scaling possibly related to the
331 rain rate. In contrast, the 03-04 September 2022 case in Fig. 2b shows parallel Ze trends between
332 the KAZR and KaSACR. The increasing Dze trend in each 6-minute period (red crosses) in Fig.
333 4d is more pronounced, indicating that the sawtooth behavior in KaSACR Ze and Dze results from
334 rainwater accumulation on the radome during the 2 minutes of vertical pointing. If the KaSACR
335 signal were saturating, it would consistently remain saturated rather than fluctuating. A closer
336 examination of XSACR Ze and Dze trends (black crosses) in Fig. 4c and d reveals minimal
337 variability with rain rates across the scanning cycle, likely due to the weaker water absorption
338 coefficient at X-band and the reduced water accumulation on the conical XSACR radome.

339 The differing KaSACR patterns between the events in Figures 2 and 4 are associated with
340 rainwater accumulation and the KaSACR/XSACR radar’s cycling between scanning and
341 stationary VPT modes. At the start of each scanning VPT period, the radome is covered by a
342 relatively thin film of rainwater, having shed water during the RHI and PPI scans. In VPT mode,
343 excess rainwater rapidly accumulates on the radome, causing increased attenuation. Consequently,
344 WRA for the KaSACR is modulated by the 10-minute scanning cycle. By contrast, during the
345 continuous stationary VPT observations of KAZR and KaSACR on 03-04 September, rainwater
346 accumulated steadily on their radomes, resulting in similar WRA patterns, and the measured Z_e
347 and Dze were parallel with a consistent offset of approximately 7 dB.

348

349 3.3 WRA Fitting Calibration Technique

350

351 In this section, we examine the WRA behavior toward developing a relative calibration
352 technique for cloud radar monitoring. Figure 5a shows the estimated Z_e by KaSACR at 500 m
353 (black cross) after gaseous and rain attenuation corrections and the corresponding VDISQUANTS-
354 estimated Z_e (red cross) as a function of R for the 03-04 September case. A very well-correlated
355 monotonic relationship between the VDISQUANTS-estimated Z_e and R in logarithmic space is
356 observed. However, the KaSACR-measured Z_e is biased low relative to the estimated Z_e , and the
357 offset ($Dze = Z_{e_{dis}} - Z_{e_{meas}}$ shown in Fig. 5b) with increasing R . The Dze approaches 0 dB at
358 $R < 0.1 \text{ mm hr}^{-1}$, when minimal WRA is expected due to the limited water on the radome.
359 However, Dze increases up to 15 dB at $R \sim 5 \text{ mm hr}^{-1}$, which is potentially a disadvantage when
360 considering cloud radar observations in precipitation. However, this characteristic range of WRA
361 relative to R provides an opportunity for exploring relative radar calibration techniques.

362 Given a quasi-linear correlation between Dze and R in logarithmic space in Fig. 5b, a
363 weighted linear least-squares fit of the Dze with R in logarithm can be applied, as described in
364 Equation 2:

365

$$366 \quad Dze = a + b \log(R) \quad (2)$$

367 For the cases shown in Fig. 5b, the fitted slope b is estimated to be 8.6. The intercept “ a ” captures
368 the radar calibration offset and the WRA when R is 1 mm hr^{-1} . Given the KaSACR calibration
369 offset is close to 0, the intercept primarily reflects WRA at this rain rate, yielding an intercept of
370 approximately 11.1 dB.

371 This log-linear relation between Dze and R is different from the $R^{1/3}$ dependence described
372 by Gibble's formula (Eq.1), which is applied by Frasier et al. (2013) and Gorgucci et al. (2013) in
373 X-band radar calibrations. Since the water absorption coefficient at Ka-band is approximately three
374 times that at X-band, we divide the result of Eq. 2 by 3 and compare it with the fitting relations
375 from Frasier et al. (2013, solid blue line) and Gorgucci et al. (2013, solid black line) in Figure 6.
376 The relationship from this study intersects with those of Frasier et al. (2013) and Gorgucci et al.
377 (2013) at $R=0.2 \text{ mm hr}^{-1}$, aligning with the majority of our data. When $R > 0.2 \text{ mm hr}^{-1}$, our WRA
378 fitting results exceed those of Gorgucci et al. (2013) by less than 0.5 dB, although Gorgucci et al.'s
379 relation is 0.5-1 dB higher than that of Frasier et al. (2013). When $R < 0.2 \text{ mm hr}^{-1}$, our WRA
380 fitting result is 0.5-1 dB lower than both previous studies. The observed differences (within 1 dB)
381 are smaller than the data scatter in Fig. 5b (standard deviation of 3 dB) and the discrepancies
382 between the two previous studies, suggesting that the log-linear fitting in Eq. 2 is suitable for WRA
383 correction when R is below 5 mm hr^{-1} , the selected threshold for our analysis. The calibration
384 offset calculation associated with the WRA fitting functions will be further examined in Section
385 4.

386
387 Assuming that radar calibration offsets are independent of R , and that WRA depends
388 intrinsically on R , the radar calibration offset can be determined by monitoring the fitted intercept
389 in Eq. 2. Figure 5e shows the fitted intercept of Dze of KAZR is 18.5 dB, about 7.5 dB higher than
390 that of KaSACR, which is consistent with the observed offset between KaSACR and KAZR in
391 Figure 1d and the time series in Figure 2c. Alternatively, we can also assume negligible WRA at
392 very low rain rates, e.g., $R = 0.05 \text{ mm hr}^{-1}$, making $Dze (R = 0.05)$ a reliable measure of the radar
393 calibration offset (C) for monitoring radar performance. For the KaSACR on 03-04 September
394 case (Fig. 5a), the $Dze (R = 0.05)$ is -0.1 dB, while for the KAZR, it is 7.3 dB, consistent with direct
395 comparisons between KaSACR, KAZR, and VDISQUANTS. This finding suggests that the WRA
396 technique provides robust offset estimates for this case. The corrected Ze values using the log-
397 linear fitted Dze in Eq. 2 are compared with VDISQUANTS Ze in Fig. 5c and 5f for KaSACR and
398 KAZR, respectively. The correlation coefficient (rr) improves to ~ 0.9 , with a mean bias of 0 dB
399 and a standard deviation of 3.0 dB for both KaSACR and KAZR.

400

401 To further explore the intrinsic WRA dependence on R , we applied the WRA log-linear
402 fitting calibration technique to KaSACR in its scanning-VPT modes. Due to water shedding during
403 the scanning cycle, we used the last-minute measurement of each 2-minute VPT period within the
404 10-minute scanning cycle. To obtain a range of samples, we identified five stratiform rain days—
405 May 25, August 5, 11, 19, and 29—and combined data from these events. The data collected from
406 those five days are plotted along with the corresponding VDISQUANTS-estimated Z_e (red cross)
407 as a function of rain rates in Fig. 5g. For these events, $Dze_{(R=0.05)}$ is -0.9 dB, with slope “b” fitted
408 to 8.6. The corrected Z_e using this log-linear fitted Dze is compared with the VDISQUANTS Z_e
409 in Fig. 7i, demonstrating a strong correlation with the reference Z_e , along with a smaller standard
410 deviation ($rr=0.91$; mean bias, 0 dB; and standard deviation, 2.0 dB).

411 Recall the $Dze_{(R=0.05)}$ of -0.1 dB for stationary VPT mode in 03-04 September case, the
412 difference between the two KaSACR offsets is less than 1 dB, which is well within the standard
413 deviation of the estimated Z_e (3 dB) as a function of R , and aligns closely with the 1 dB offset
414 from the direct disdrometer comparison at light rain onset in Fig. 2. This suggests that the R
415 dependence of WRA is a valid assumption, therefore the interceptor or $Dze_{(R=0.05)}$ in the fitting of
416 Eq. 2 can be a useful metric for radar offset monitoring.

417 The time and height plots of Z_e from KaSACR, XSACR, and KAZR GE and MD modes
418 on 03-04 September 2022 (after the WRA correction is applied) are shown in Figure 7. For the
419 precipitating period, KaSACR is adjusted with Eq. 2 with a slope of 8.6 and constant of 11.1 (Table
420 2 or Fig. 5b). XSACR is modified with the offset of 3 dB from VDISQUANTS (black cross in Fig
421 2d), and KAZR GE mode is corrected using Eq. 2 with a slope of 8.6 and an intercept of 18.5
422 (Table 2, or Fig. 5b). For non-precipitating periods, the calibration offsets for KaSACR and
423 XSACR are assumed to be 0 dB based on the previous discussion, while the KAZR GE mode is
424 calibrated with an offset of 7 dB. In contrast to the apparent difference of more than 5 dB between
425 KAZR and KaSACR shown in Figure 1, the corrected Z_e values from KAZR and KaSACR are
426 comparable to those from XSACR in cloud and light rain conditions. Under the relatively heavy
427 rain conditions (e.g., 2330 UTC), XSACR Z_e along the fall streaks maintains magnitudes near 30
428 dBZ from the surface up to the melting layer, while Z_e estimates from KAZR and KaSACR
429 gradually decrease from the surface to the melting layer, likely due to increasing attenuation in
430 Ka-band observations. This comparison in Figure 7 further supports the applicability of the WRA

431 fitting technique to KAZR measurements and KaSACR in VPT modes, providing reasonable
432 estimates for wet-radome corrections during precipitation and radar offset monitoring.

433

434 4 Application and Evaluation of the WRA Offset Monitoring During TRACER

435 4.1 Daily TRACER KAZR Calibration Offset Applications

436

437 We apply the WRA fitting technique on the Dze and R relationship using VDISQUANTS
438 Ze estimates versus KAZR Ze for each day with measured precipitation throughout TRACER
439 campaign. The fitted slopes from the daily events typically range from 6 to 10, with rr generally
440 exceeding 0.7. The fitted slopes and associated fitting errors depend on the distribution of data
441 samples. For example, in rain events with short durations or limited variability in intensity, data
442 samples may cluster within a narrower range, resulting a relatively lower correlation coefficient
443 between the fitted Ze and disdrometer Ze , potentially indicating less reliable results.

444

445 To mitigate uncertainty associated with “daily” fitting as above, one may assume that the
446 Dze and R relation has a constant slope over longer windows. In this study we consider applying
447 the WRA fitting technique with an average slope of 8, selected as a representative value for
448 extended rain conditions across the entire TRACER campaign dataset. As a sensitivity study of
449 this composite slope, we conduct offset calculations with proxy slope values at 6, 8 and 10 for both
450 KAZR and KaSACR in the 03-04 September 2022 case. Table 2 presents the results of these tests.
451 As the slopes increase from 6 to 10, the calibration offsets for both KAZR and KaSACR decrease
452 by approximately 3 dB, as expected. With increasing slope values, the least-squares fit prioritizes
453 the data samples around 0.1 - 1 mm hr⁻¹, resulting in a mathematical decrease in C .

454 To further illustrate, we applied the WRA fitting with a slope of 6 to the KaSACR
455 observations in Figure 5a. The fitted relation is represented by the red dashed line in Figure 6. It
456 can be seen that the fitted Ze with a slope of 6 lies between the results from Frasier et al. (2013)
457 and Gorgucci et al. (2013). For most data samples (concentrated around 0.1 - 1 mm hr⁻¹), the
458 difference between the two WRA fitting results remains within 1 dB. The resulting C with slope
459 of 6 is larger than that with a slope of 8. However, the offset deviation due to possible fitting slope
460 fitting changes (shown in Table 2) is 3 dB, which is within the standard deviation of the estimated
461 Ze as a function of R (~3 dB). Therefore, even with fitting slope errors associated with this relative

462 WRA technique, drifts larger than the 3 dB in the long-term calibration trend would be meaningful
463 and identifiable.

464 The calculated KAZR calibration offsets during the entire TRACER campaign are shown
465 in Fig. 8a (black asterisk for the daily value, thin dash line representing the mean campaign-wide
466 trend). The calibration offsets remain relatively stable around 2 dB, with a standard deviation of 3
467 dB until 1 July 2022 (273 days since 1 Oct. 2021 in Fig. 8). After this date, the calibration offset
468 increases to around 7 dB in September. This shift is larger than the uncertainty of the fitting method
469 and the standard deviation of the fitting data, which is found to be linked to a drop of about 1 dB
470 in transmitter power toward the end of the project in TRACER radar b1 data processing (Feng et
471 al., 2024) and in Figure 9c.

472
473

474 4.2 Evaluation of the TRACER KAZR Calibration Trend

475 By monitoring the $Dze_{(R=0.05)}$ from each rainy day that meets our stratiform and duration
476 selection criteria, we determine a relative radar calibration offset trend. This offset includes
477 additional uncertainty due to fitting uncertainty and the assumption of negligible WRA at $R \sim 0.05$
478 mm hr^{-1} . Combining this WRA fitting technique with other, typically less frequent, absolute radar
479 calibration references would be ideal and cost-effective for KAZR long-term calibration. To
480 evaluate the KAZR calibration offset trend over the entire TRACER campaign, we performed
481 three separate tests to demonstrate the potential offset uncertainty and/or advantages of the current
482 WRA fitting technique compared to other established methods.

483

484 4.2.1 Direct KAZR-Disdrometer Comparison Near to Light Rain Onset

485 As previously noted, a wet radome film may not form immediately at the onset of light
486 rain, so WRA is often assumed to be negligible when calibrating radar using disdrometer
487 measurements near these rain onset windows. We perform a direct KAZR-disdrometer comparison
488 at or near light rain onset for qualifying KAZR calibration events. The onset mean offset for each
489 day is calculated if there are data samples with $R < 0.1 \text{ mm hr}^{-1}$ lasting for 5 consecutive minutes
490 within each observed rain event. The onset mean offsets are shown in Fig. 8a (red diamonds). For
491 days with an onset mean offset, these values are typically close to those calculated using the WRA
492 fitting technique. However, this method's applicability depends on the variation in precipitation

493 rate over the 5-minute sampling period and the minimum sensitivity of VDISQUANTS. The
494 former introduces large uncertainty, while the latter limits the number of data samples, as shown
495 in Fig. 8a.

496

497 *4.2.2 WRA Fitting Technique Against the Calibrated RWP Ze*

498 As an independent cross-comparison, we also apply the WRA fitting technique with respect
499 to calibrated RWP Ze at RWP time resolution (less than 8 seconds), using interpolated disdrometer
500 rain rates over the entire TRACER campaign. Here, Dze is replaced by the difference between
501 KAZR and RWP measurements. The WRA calibration offsets using RWP measurements are
502 shown with black asterisks in Fig. 8b. First, we observe fewer available RWP data points, due to
503 RWP mode switching during transient rain events. For days with available RWP measurements,
504 the calibration offsets closely align with those derived using disdrometer-estimated Ze in Fig. 8a
505 and direct disdrometer comparisons. The offset trend drift from early July to September is
506 smoother and more clearly defined than the trend observed with disdrometer measurements, likely
507 due to better temporal resolution. Overall, the consistency in temporal trend and magnitude of
508 calibration offsets between disdrometer and RWP measurements indicates strong performance of
509 the new WRA fitting technique.

510

511 *4.2.3 Cross-Comparison Between KaSACR and KAZR*

512 As previously mentioned, KaSACR calibration offsets remained stable between May and
513 September 2022. Furthermore, its calibration offsets, calculated from the WRA fitting technique
514 with scanning VPT and stationary VPT measurements in Fig. 6, are approximately -0.9 to -0.1 dB,
515 respectively, and around 1 dB from direct disdrometer comparison at light rain onset. We
516 tentatively assign a calibration offset of 0 dB for KaSACR observations. Cross-comparison
517 between KaSACR VPT mode and KAZR observations can then be used to quantify the KAZR
518 calibration offset trend. Since KaSACR and KAZR operate at the same frequency, this cross-
519 comparison uses full-profile samples rather than measurements at a specific height level, as
520 cumulative gaseous and rain attenuation should be consistent across range gates.

521 For this cross-comparison, we first match the closest KaSACR profiles to KAZR profiles
522 and interpolate KaSACR height ranges to align with KAZR height ranges. We then select data
523 samples using a signal-to-noise ratio threshold of 5 dB for both KaSACR and KAZR. In

524 precipitating events, KaSACR in scanning VPT mode is expected to exhibit a sawtooth or
525 modulated WRA cycling behavior, while KAZR VPT operates under consistent/continuous WRA
526 (see Fig. 2). We categorize the collocated profiles into precipitating and non-precipitating periods
527 using collocated surface rain rates from disdrometer measurements. Finally, the daily mean offsets
528 between KaSACR and KAZR observations in non-precipitating clouds are calculated and shown
529 in Fig. 8b (red diamonds). These calculated offsets display a trend similar to that observed from
530 the WRA fitting technique against RWP measurements in Fig. 8b, further supporting the validity
531 of the WRA calibration offset behaviors and strengthening confidence in the offset drift observed
532 at the end of the campaign.

533 To extend the method to different disdrometer setups, we applied the WRA fitting
534 technique to LDQUANTS estimates. Additionally, we tested sensitivity to fitting functions of log-
535 linear and $R^{1/3}$ dependencies to account for potential discrepancies. Figures 9a and 9b present the
536 results with a 2-day running average. The daily calibration offsets show slight variations between
537 LDQUANTS and VDISQUANTS, indicating minor differences in disdrometer measurements
538 (Wang et al. 2021). While the calibration offsets from the log-linear and $R^{1/3}$ fittings can differ by
539 up to 2 dB for certain day, the overall trends remain similar, with a mean offset of approximately
540 2 dB before July 2022, increasing to around 7 dB afterward. The increase of calibration offsets is
541 well correlated with the noticeable decrease of transmitted power (Figure 9c) observed at the end
542 of the project.

543 5 Summary

544 In this study, we have demonstrated the wet radome influence on Ka-band radar
545 observations through comparisons that included KaSACR VPT observations under scanning (that
546 may shed water buildup) and stationary (non-shedding) conditions. The WRA is attributed to both
547 wet film and cumulative rainwater collecting on the radar radome. This attenuation influence
548 increases, as the rain rate increases. In campaign settings, it was found this attenuation may exceed
549 10 dB under a modest rain rate of 5 mm hr^{-1} . Taking advantage of the intrinsic WRA dependence
550 on rain rates as obtained in moderate rain events from the AMF1 deployment in Houston, TX
551 during the TRACER field campaign, a new relative calibration monitoring technique was
552 developed for use with the ARM KAZR (or similar cloud radar systems) observations.

553 The well-correlated relation between Dze and R (in logarithmic space) on precipitating
554 days is fitted with a log-linear equation. This rain dependence of WRA serves as the basis for this
555 relative WRA calibration technique. The corrected KAZR Ze with fitted Dze , which includes the
556 WRA and Ze offset, agrees very well with both disdrometer-estimated and RWP-measured Ze .
557 The radar calibration offset is calculated from the fitted Dze - R relation when R equals 0.05 mm
558 hr^{-1} , assuming WRA is negligible at this light rain rate. The daily fitted slopes over the course of
559 the TRACER campaign vary between 6 and 10 due to different data sampling in different rain
560 types. A slope sensitivity study suggests that the calibration offset deviations due to slope variation
561 are likely within the standard deviation of the estimated Ze as function of R , as well as those typical
562 of underlying/collocated disdrometer measurement uncertainty (i.e. $\sim 2\text{-}3 \text{ dB}$). The KAZR
563 calibration offsets calculated with a constant slope of 8 during the TRACER campaign are stable
564 near 2 dB compared to the disdrometer estimate with a standard deviation of 3 dB through June
565 2022. After that time, the calibration offsets increase to more than 7 dB.

566 The performance of the WRA fitting calibration technique is evaluated by comparing it
567 with direct disdrometer measurements at the onset of rain events. The wet-radome technique
568 consistently identifies a sound calibration offset over the entire project and arguably outperforms
569 the direct disdrometer and radar comparison at the onset of light rain by reducing noise and
570 increasing temporal consistency. The WRA fitting calibration technique is also applied to the
571 KAZR observation against the calibrated RWP Ze reference. This test reveals sound performance
572 and a clear and smooth matching trend in the July to September change in TRACER KAZR offsets,
573 indicating that the new technique can be applicable to other calibrated reference radars with
574 collocated surface rain rate measurements. The KAZR offset assessed from the cross-comparison
575 between the stable and calibrated KaSACR VPT mode and KAZR observations in non-
576 precipitating clouds also agree with the calibration offset trend from the WRA fitting technique.
577 The daily calibration offsets vary due to the uncertainty of disdrometer measurements and the
578 fitting function of WRA, however the generally long-term trend from the WRA fitting technique
579 seems robust.

580

581 Determining the calibration offset and monitoring the long-term trend of ARM KAZR is
582 the first step towards studying cloud seasonal and inter-seasonal variation. Having an easily
583 adjustable cloud radar calibration method with collocated disdrometer or RWP data available will

584 also facilitate cloud microphysical property retrieval, cloud process studies, and cloud variation
585 associated with climate change using ARM KAZR measurements. This technique has the
586 advantage of utilizing data from a broader range of light and moderate rain cases, avoiding the
587 stringent requirements of other shorter-wavelength radar monitoring methods, which often rely on
588 disdrometers or other radars and require observations of cloud, drizzle, or light rain at the onset of
589 precipitation. Future plans include testing this newly developed WRA technique at other ARM
590 fixed sites (e.g., in more humid, marine, or oceanic environments) to assess the extent of any
591 necessary site-specific refinements for different radar and sampling conditions. Recently, this
592 WRA monitoring technique has been applied to data from other ARM field campaigns, such as
593 the Surface Atmosphere Integrated Field Laboratory (SAIL) and the Eastern Pacific Cloud Aerosol
594 Precipitation Experiment (EPCAPE). Alongside TRACER, the offset trends derived from these
595 three campaigns have shown favorable agreement with results from other independent KAZR
596 calibration techniques documented in ARM radar b1 data processing reports (Feng et al., 2024;
597 Matthew et al., 2024; Rocque et al., 2024).

598

599

600

601

602

603

604

605

606

607

608

609

610

611

612

613

614

615 Table 1. List of parameters for KAZR GE mode, KaSACR/XSACR in vertical pointing (VPT)
 616 mode, and RWP in precipitation mode.

617

| | KAZR (GE mode) | KaSACR (VPT mode) | XSACR (VPT mode) | RWP (Precipitation mode) |
|-------------------------|----------------------|----------------------|---------------------|--------------------------------|
| Frequency (GHz) | 34.0 | 35.3 | 9.71 | 1.29 |
| Wavelength | 8.57mm | 8.50mm | 3.09cm | 23.3cm |
| Beam width (degree) | 0.3 | 0.3 | 1.0 | >3 |
| Time resolution (s) | 2 | 4 | 3 | 5-8 |
| Range resolution (m) | 30 | 25 | 25 | 225 |
| Minimum range (m) | 160 | Others: 428 | 288 | 335 |
| | | 0903/04: 453 | | |
| Radome diameter (m) | 1.82 | 1.82 | 1.82 | N/A |

618

619

620

621

622

623

624

625

626

627

628

629

630

631

632

633

634

635

636

637

638

639

640

641 Table 2. Sensitivity study of the slope value in the log-linear fitting for KAZR and KaSACR
 642 calibration on 03-04 September 2022 case in Figure 1. b and a are the slope and constant,
 643 respectively, in the log-linear fitting in Eq. 2. $D_{Ze}(R=0.05)$ is the radar calibration offset when rain
 644 rate (R) equals 0.05 mm hr^{-1} . More details can be found in Section 3.3.

645

| | KAZR | | | | KaSACR | | | |
|-----|------|--------------------------|--|-------------------------------|--------|--------------------------|--|-------------------------------|
| b | a | D_{Ze} ($R=0.05$) | Correlation coefficient (rr) | Standard deviation (dB) | a | D_{Ze} ($R=0.05$) | Correlation coefficient (rr) | Standard deviation (dB) |
| 6 | 17.1 | 9.3 | 0.88 | 3.8 | 9.8 | 2.0 | 0.89 | 3.4 |
| 8 | 18.1 | 7.7 | 0.90 | 3.9 | 10.9 | 0.5 | 0.91 | 3.4 |
| 8.6 | 18.5 | 7.3 | 0.91 | 4.1 | 11.1 | -0.1 | 0.92 | 3.5 |
| 10 | 19.1 | 6.3 | 0.92 | 4.4 | 12.0 | -1.0 | 0.93 | 3.7 |

646

647

648

649

650

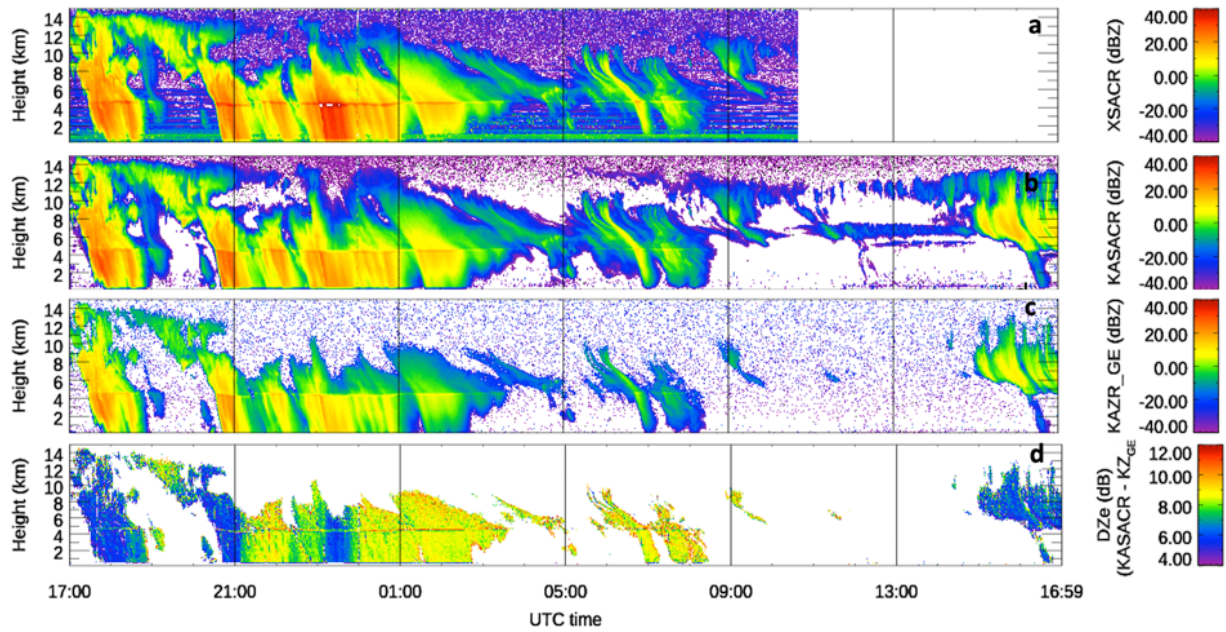
651

652

653

654

655



656

657 Figure 1. Measured radar reflectivity on 03-04 September 2022 from the TRACER field campaign.

658 a) XSACR, missing data after 10:40 UTC on 04 September 2022, b) KaSACR, c) KAZR GE mode,

659 d) Ze difference (DZe) between the KaSACR and the KAZR GE mode.

660

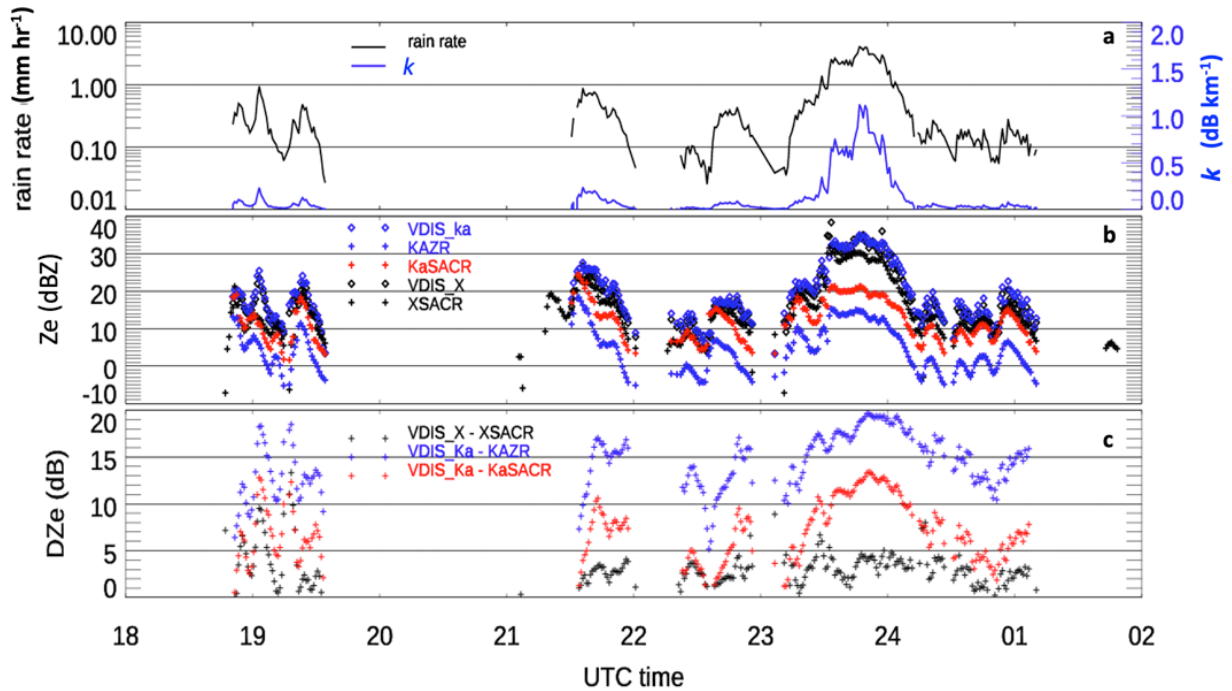
661

662

663

664

665



666

667

668 Figure 2. Measurements and comparison on 03-04 September 2022 between VDISQUANTS and
 669 radars. a) the timeseries of VDISQUANTS rain rate (black line) and rain droplet specific
 670 attenuation coefficients (K , blue line) at Ka band. b) the time series of measured Z_e from KAZR
 671 GE (blue +), KaSACR (red +), and XSACR (black +) at 500 m after gaseous and rain attenuation
 672 corrections, and estimated Z_e from VDISQUANTS at Ka (blue diamond) and X (black diamond)
 673 bands. c) Z_e difference (DZe) between radar and disdrometer for XSACR (black cross), KaSACR
 674 (read cross), and KAZR (blue cross). For this case, SACR was operated in the stationary VPT
 675 mode.

676

677

678

679

680

681

682

683

684

685

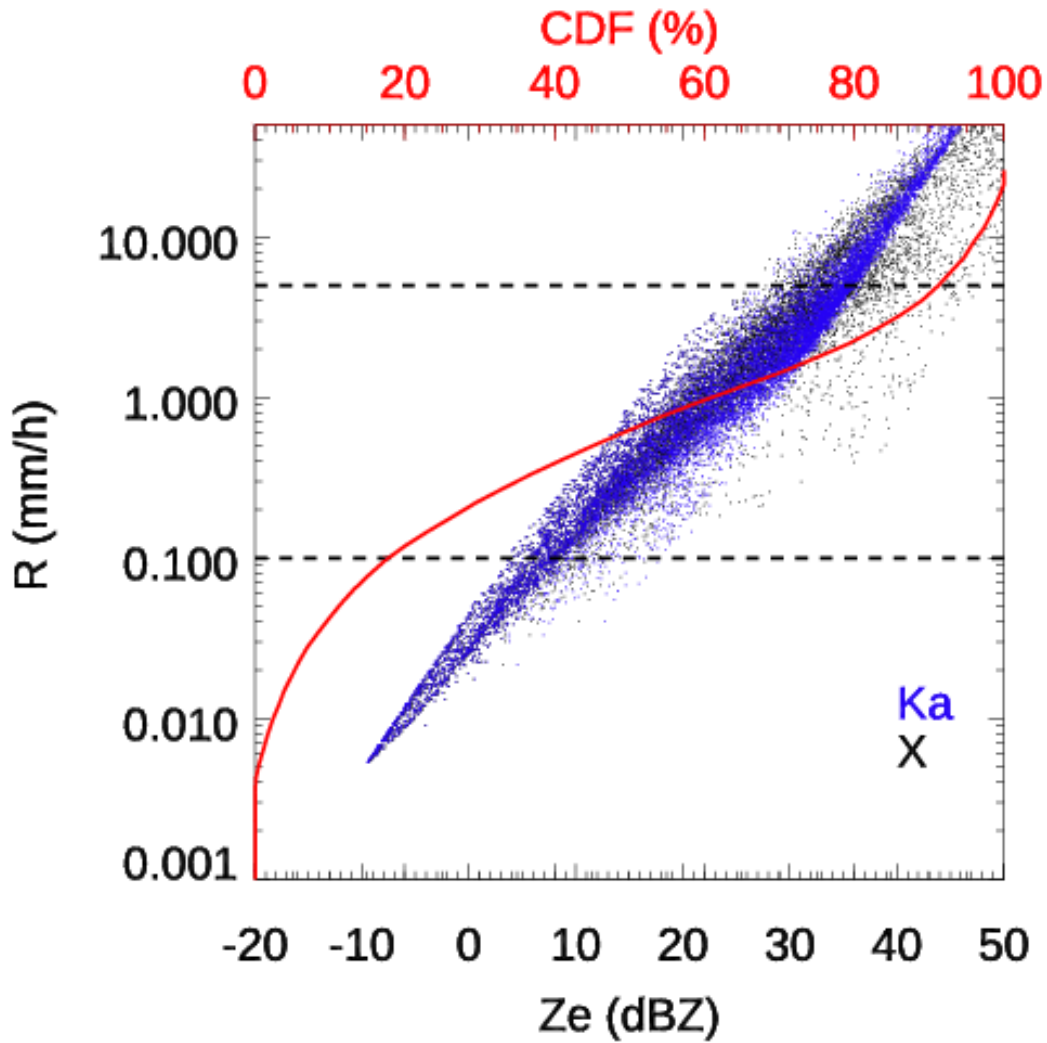
686

687

688

689

690

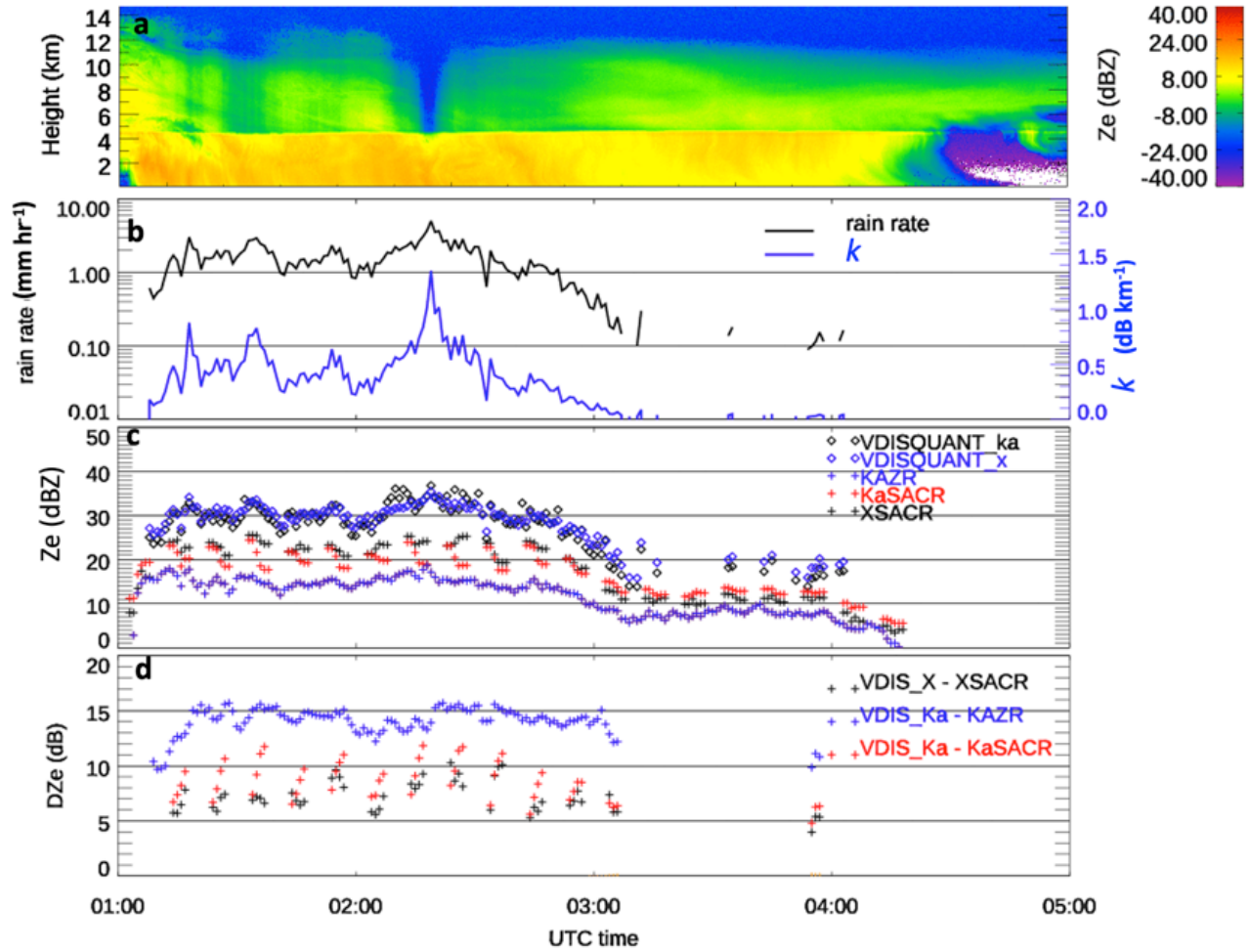


691

692 Figure 3. The estimated Z_e from VDISQUANTS for Ka (blue dots) and X bands (black dots)
693 during the entire TRACER campaign, plotted as a function of rain rate (R). The red line is the
694 cumulative probability function (CDF) of R . The two vertical black lines are at rain rates of 0.1
695 and 5.0 mm hr⁻¹, respectively.

696

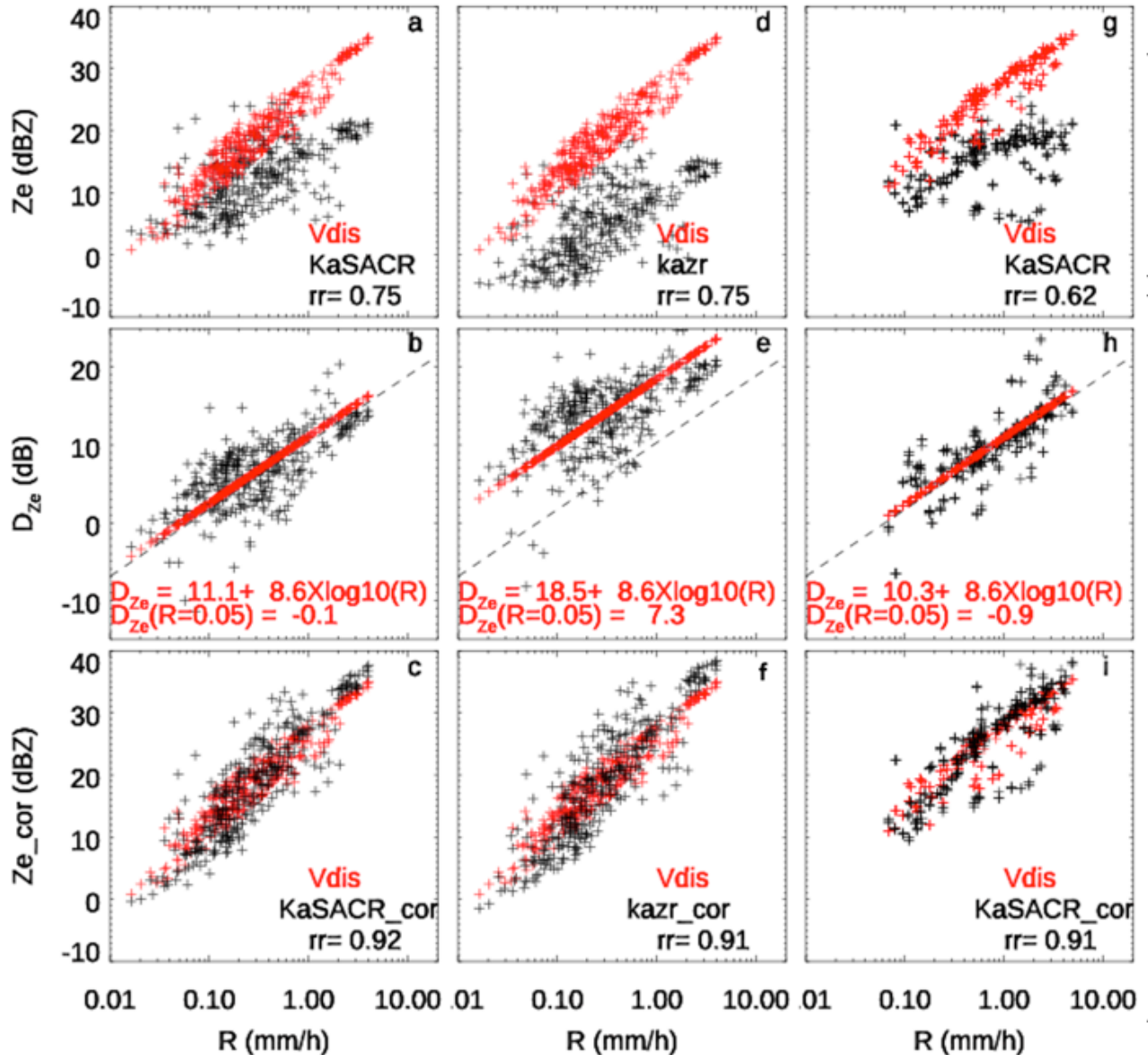
697



698

699 Figure 4. Radar and VDISQUANTS comparison for the case on August 11. a) Measured radar
 700 reflectivity (Z_e) from the KAZR GE mode. b-d are similar to Fig. 2a-c. For this case, KaSACR
 701 and XSACR measurements are the scanning VPT mode and collocated with the VDISQUANTS
 702 with a ± 2 minutes averaging window.

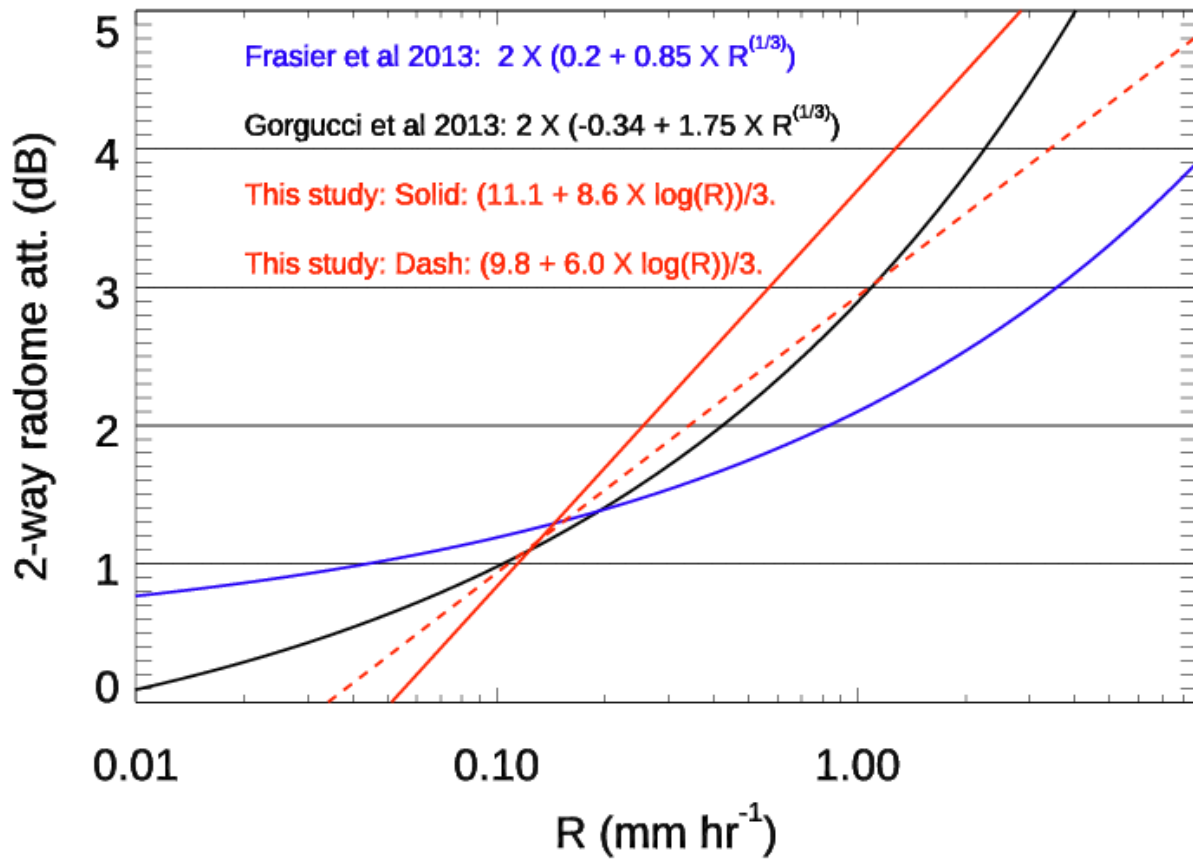
703



704

705 Figure 5. a) Scatter plot of radar measured Z_e (black cross) at 500 m and VDISQUANTS-estimated
 706 Z_e (red cross) as a function of rain rate R , b) Difference between measured Z_e and VDISQUANTS-
 707 estimated Z_e (D_{ze} in black). The log-linear fitting in Eq. 2 with slope b at 8.6 are plotted in red
 708 cross, c) Scatter plot of radar measured Z_e (black cross) after log-linear fitting correction along
 709 with the VDISQUANTS-estimated Z_e (red cross) for KaSACR stationary VPT (a-c) and KAZR
 710 GE (d-f) on 03-04 September, and KaSACR stationary VPT (g-i) collected on May 25, August 05,
 711 11, 19 and 29. The correlation coefficients between the measured Z_e and estimated Z_e (rr) before
 712 and after the fitting correction are noted. The dashed black lines in second row (b, e, h) are the log-
 713 linear fitting with $a=10.3$ and $b=8.6$ for KaSACR in Table 2.

714
715
716
717



718

719 Figure 6. Two-way radome attenuation as a function of rain rate (R) using the log-linear WRA
720 fitting relation in Eq. 2 with slopes of 8.6 (solid red) and 6.0 (dashed red) in this study at Ka-band,
721 which is divided by 3 and compared with two previous studies about X-band radars from Frasier
722 et al. 2013 and Gorgucci et al. 2013.

723

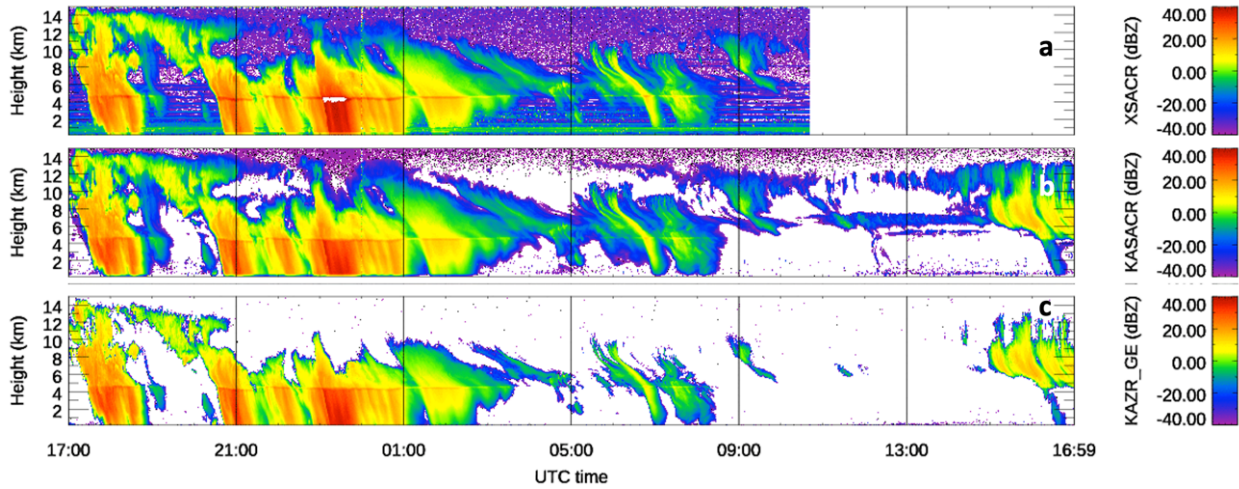
724

725

726

727

728



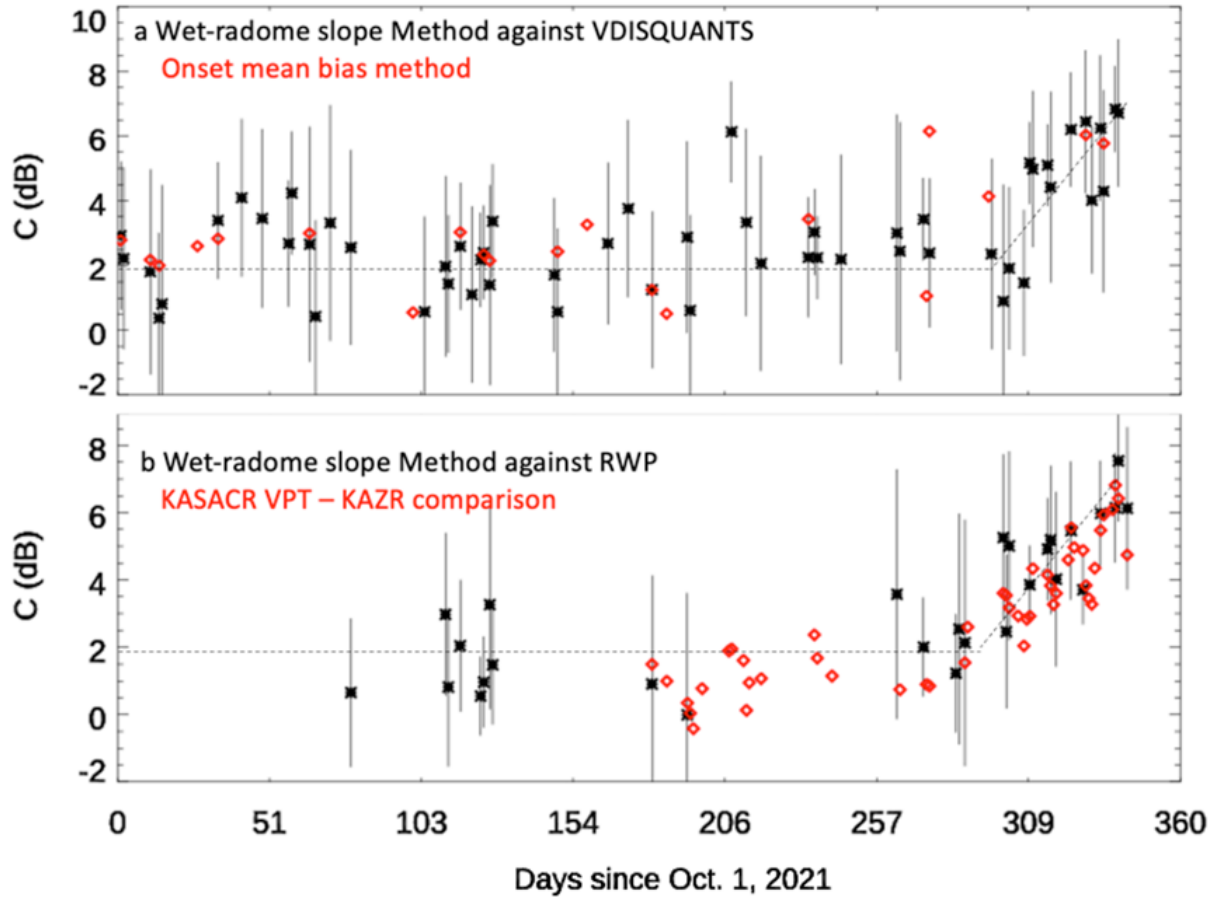
729

730 Figure 7. The same as Figure 1a-c except after WRA correction and radar calibration. For the
731 precipitating period, KaSACR is corrected using Eq. 2, with a slope of 8.6 and constant of 11.1.
732 XSACR is corrected with the offset of 3 dB from VDISQUANTS (black cross in Fig 2d), and
733 KAZR GE mode is corrected using Eq. 2, with a slope of 8.6 and constant of 18.5. For non-
734 precipitating periods, the calibration offsets of KaSACR and XSACR are assumed to be 0 dB,
735 while the KAZR GE mode is calibrated with offset of 7 dB.

736

737

738



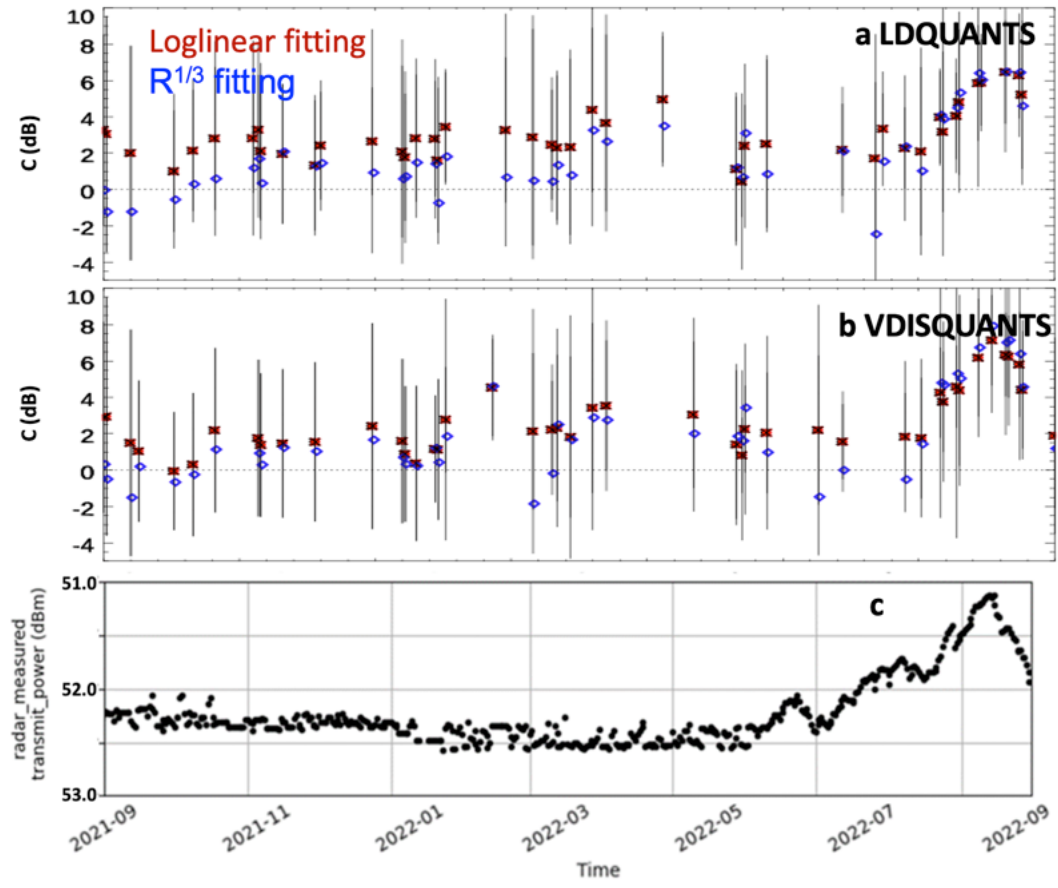
739
740

741 Figure 8. a) KAZR daily calibration offsets (C) from the mean KAZR bias method at the onset of
742 light rain (red diamond) and the WRA fitting technique (black asterisk) against the VDISQUANTS
743 data. Black vertical bar is the standard deviation of corrected Z_e against the estimated Z_e . b) KAZR
744 daily calibration offset from the WRA fitting technique against the calibrated RWP measurement
745 in black asterisk with vertical standard deviation bar. Red diamonds stand for the daily cross-
746 comparison between the KaSACR VPT mode and the KAZR GE mode in non-precipitating clouds
747 since May 26, 2022. The dashed black line is the mean trend outline from the WRA fitting
748 technique in Fig. 8a.

749

750

751



752

753 Figure 9 KAZR daily calibration offsets (C) from log-linear fitting with Eq. 2 (red asterisk with
 754 black standard deviation bar) or the $R^{1/3}$ relation (blue diamond) against a) LDQUANTS and b)
 755 VDISQUANTS data. The daily offsets are smoothed with 2-day window. c) KAZR transmitted
 756 power. Noticeable decrease of transmitted power is well correlated with the increase of calibration
 757 offset.

758

759

760

761

762

763 Data availability

764

765 The KAZR, KaSACR and XSACR data at the TRACER campaign in this study are a1-level data.
766 The surface disdrometer VDISQUANTS and interpolated sounding data are c1-level value added
767 product data. They are all available at ARM data discovery at <https://adc.arm.gov/discovery/#/> and
768 through the following DOIs. The calibrated radar wind profiler data is ARM PI product and can
769 be obtained from the data developer, Dr. Christopher R. Williams, through email
770 (christopher.williams@colorado.edu) contact.

771

772 Bharadwaj, Nitin, Hardin, Joseph, Isom, Bradley, Johnson, Karen, Lindenmaier, Iosif, Matthews,
773 Alyssa, Nelson, Danny, Feng, Ya-Chien, Deng, Min, Rocque, Marquette, Castro, Vagner,
774 and Wendler, Tim. *Ka-Band Scanning ARM Cloud Radar*. United States: N. p., 2021. Web.
775 doi:10.5439/1469302.

776 Bharadwaj, Nitin, Hardin, Joseph, Isom, Bradley, Johnson, Karen, Lindenmaier, Iosif, Matthews,
777 Alyssa, Nelson, Danny, Feng, Ya-Chien, Deng, Min, Wendler, Tim, Castro, Vagner, and
778 Rocque, Marquette. *X-Band Scanning ARM Cloud Radar*. United States: N. p., 2021. Web.
779 doi:10.5439/1469303.

780 Hardin, Joseph, Giangrande, Scott, and Zhou, Aifang. *ldquants*. United States: N. p., 2019. Web.
781 doi:10.5439/1432694.

782 Hardin, Joesph, Giangrande, Scott, Fairless, Tami, and Zhou, Aifang. *vdisquants: Video*
783 *Distrometer derived radar equivalent quantities. Retrievals from the VDIS instrument*
784 *providing radar equivalent quantities, including dual polarization radar quantities (e.g.,*
785 *Z, Differential Reflectivity ZDR)*. United States: N. p., 2021. Web. doi:10.5439/1592683.

786 Isom, Bradley, Nelson, Danny, Andrei, Iosif, Hardin, Joseph, Matthews, Alyssa, Johnson, Karen,
787 Bharadwaj, Nitin, Feng, Ya-Chien, Rocque, Marquette, Deng, Min, Wendler, Tim, and
788 Castro, Vagner. *ARM: KAZRCFRGE*. United States: N. p., 2018. Web.
789 doi:10.5439/1498936.

790 Isom, Bradley, Nelson, Danny, Andrei, Iosif, Hardin, Joseph, Matthews, Alyssa, Johnson, Karen,
791 Bharadwaj, Nitin, Feng, Ya-Chien, Rocque, Marquette, Deng, Min, Wendler, Tim, and
792 Castro, Vagner. *ARM: KAZRCFRMD*. United States: N. p., 2018. Web.
793 doi:10.5439/1498948.

794 Jensen, Michael, Giangrande, Scott, Fairless, Tami, and Zhou, Aifang. *interpolatedsonde*. United
795 States: N. p., 1998. Web. doi:10.5439/1095316.

796

797

798

799

800

801

802

803

804

805

806

807

808

809

810

811

812

813

814

815

816

817

818

819

820

821

822

823

824

825 Author contribution

826 MD developed the main concept for the WRA calibration technique and led the manuscript
827 preparation. SG, MJ, and KJ contributed to the data analysis process. CW provided the
828 calibrated RWP data and contributed to its analysis and write-up. JC, YF, AM, MR, and
829 MD, as part of the ARM radar data mentor team, provided TRACER-related radar
830 information and additional KAZR calibration used in TRACER b1 data processing. IL and
831 TW, as ARM radar engineers, supplied critical information on radar hardware, software,
832 and radar saturation. AZ and DW contributed as the disdrometer mentors and VAP
833 developers. ZZ and EL provided valuable insights regarding radar wet radome attenuation.
834 All coauthors helped to edit and comment the manuscript draft.

835

836 Competing interests

837 The authors declare that they have no conflict of interest.

838

839

840

841

842

843

844

845

846

847

848

849

850

851

852

853

854

855 Acknowledgement

856

857 We acknowledge the exceptional work of the radar engineering team and data mentor team for the
858 close to 100% operation rate of KAZR during the TRACER campaign. We would like to thank
859 the ARM TRACER team for the quality data of KaSACR, XSACR, disdrometer, RWP and
860 interpolated sounding measurements. Contributions from Brookhaven National Laboratory co-
861 authors were supported by the Atmospheric Radiation Measurement (ARM) Facility and the
862 Atmospheric System Research (ASR) program of the Office of Biological and Environmental
863 Research in the U. S. Department of Energy, Office of Science, through Contract No. DE-
864 SC0012704. Dr. C.R. Williams and the RWP work is supported under ASR grant number DE-
865 SC0021345. Pacific Northwest National Laboratory (PNNL) is operated by Battelle for the U. S.
866 Department of Energ. The authors from PNNL are also supported by ARM through Contract
867 No. DE-SC0015990.

868

869 Reference

870 Anderson, I., 1975: Measurements of 20-GHz transmission through a radome in rain. *IEEE Trans.*
871 *Antennas Propag.*, 23, 619–622.

872 Baldini, L., V. Chandrasekar, and Dmitri Moisseev 2012: Microwave radar signatures of
873 precipitation from S band to Ka band: application to GPM mission, *International Journal*
874 *of Remote Sensing*, Volume 41, 2020 - Issue 13, <https://doi.org/10.5721/EuJRS20124508>

875 Bertie J. E.; Lan Z. (1996). "Infrared Intensities of Liquids XX: The Intensity of the OH Stretching
876 Band of Liquid Water Revisited, and the Best Current Values of the Optical Constants of
877 H₂O(l) at 25°C between 15,000 and 1 cm⁻¹". *Applied Spectroscopy*. 50 (8): 1047-
878 1057. doi:10.1366/0003702963905385. S2CID 97329854.

879 Bringi, V. N, V Chandrasekar, N Balakrishnan, and DS Zrníc. 1990. "An Examination of
880 Propagation Effects in Rainfall on Radar Measurements at Microwave Frequencies."
881 *Journal of Atmospheric and Oceanic Technologies* 7(6): 829–840,
882 [https://doi.org/10.1175/1520-0426\(1990\)0072.0.CO;2](https://doi.org/10.1175/1520-0426(1990)0072.0.CO;2)

883 Bringi, V. N., and Chandrasekar V., 2001: Polarimetric Doppler Weather Radar. Cambridge
884 University Press, 636 pp.

885 Bechini, R., V. Chandrasekar, R. Cremonini, and S. Lim, 2010: Radome attenuation at X-band
886 radar operations. Proc. Sixth European Conf. on Radar in Meteorology and Hydrology,
887 Sibiu, Romania, ERAD, P15.1.

888 Bringi, V. N, Kumar Vijay Mishra, Merhala Thurai, Patrick C. Kennedy, and Timothy H. Raupach
889 2020: Retrieval of Lower-Order Moments of the Drop Size Distribution using CSU-CHILL
890 X-band Polarimetric Radar: A Case Study. Atmospheric Measurement Techniques.
891 <https://doi.org/10.5194/amt-2020-160>

892 Chandrasekar, V, L Baldini, N Bharadwaj, and PL Smith. Recommended Calibration Procedures
893 for GPM Ground Validation Radars, 103.

894 Deng, M., and Pavlos Kollias, Zhe Feng, Chidong Zhang, Charles N. Long, Heike
895 Kalesse, Arunchandra Chandra, Vickal V. Kumar, and Alain Protat, 2014: Stratiform and
896 Convective Precipitation Observed by Multiple Radars during the DYNAMO/AMIE
897 Experiment. J. Appl. Meteor. Climatol., 53, 2503–2523, [https://doi.org/10.1175/JAMC-D-](https://doi.org/10.1175/JAMC-D-13-0311.1)
898 13-0311.1.

899 Feng, Y-C, A Matthews, M Rocque, M Deng, T Wendler, K Johnson, E Schuman, I Lindenmaier,
900 V Castro, SE Giangrande, S Collis, R Jackson, A Theisen, and J Comstock. 2024.
901 TRACER b1 Data Processing: Corrections, Calibrations, and Processing Report. U.S.
902 Department of Energy, Atmospheric Radiation Measurement user facility, Richland,
903 Washington. DOE/SC-ARM-TR-297.

904 Frasier, S. J., F. Kabeche, J. Figueras i Ventura, H. Al-Sakka, P. Tabary, J. Beck, and O. Bousquet,
905 2013: In-Place Estimation of Wet Radome Attenuation at X Band. J. Atmos. Oceanic
906 Technol., 30, 917–928, <https://doi.org/10.1175/JTECH-D-12-00148.1>.

907 Frech, M., Lange, B., Mammen, T., Seltmann, J., Morehead, C., & Rowan, J. (2013). Influence of
908 a Radome on Antenna Performance, Journal of Atmospheric and Oceanic

909 Technology, 30(2), 313-324. Retrieved Mar 6, 2023,
910 from https://journals.ametsoc.org/view/journals/atot/30/2/jtech-d-12-00033_1.xml

911 Gibble, D., 1964: Effect of rain on transmission performance of a satellite communication system.
912 IEEE International Convention Record, Part VI, IEEE, 52.

913 Giangrande, S. E., and A. V. Ryzhkov, 2005: Calibration of Dual-Polarization Radar in the
914 Presence of Partial Beam Blockage. *J. Atmos. Oceanic Technol.*, 22, 1156–1166,
915 <https://doi.org/10.1175/JTECH1766.1>.

916 Giangrande, S. E., E. P. Luke and P. Kollias, 2010: Automated retrievals of precipitation
917 parameters using non-Rayleigh scattering at 95 GHz. *J. Atmos. Oceanic Technol.*, 27,
918 1490–1503.

919 Giangrande, S. E., E. P. Luke, and P. Kollias, 2012: Characterization of Vertical Velocity and
920 Drop Size Distribution Parameters in Widespread Precipitation at ARM Facilities. *J. Appl.*
921 *Meteor. Climatol.*, 51, 380–391, <https://doi.org/10.1175/JAMC-D-10-05000.1>.

922 Giangrande, S. E., S. Collis, J. Straka, A. Protat, C. Williams, and S. Krueger (2013), A summary
923 of convective-core vertical velocity properties using ARM UHF wind profilers in
924 Oklahoma, *J. Appl. Meteorol. Climatol.*, 52, 2278–2295.

925 Giangrande, S. E., Toto, T., Jensen, M. P., Bartholomew, M. J., Feng, Z., Protat, A., Williams, C.
926 R., Schumacher, C., and Machado, L. (2016), Convective cloud vertical velocity and mass-
927 flux characteristics from radar wind profiler observations during GoAmazon2014/5, *J.*
928 *Geophys. Res. Atmos.*, 121, 12,891–12,913, doi:10.1002/2016JD025303.

929 Giangrande, S. E., Wang, D., Bartholomew, M. J., Jensen, M. P., Mechem, D. B., Hardin, J. C., &
930 Wood, R. (2019). Midlatitude oceanic cloud and precipitation properties as sampled by the
931 ARM Eastern North Atlantic Observatory. *Journal of Geophysical Research: Atmospheres*,
932 124, 4741–4760. <https://doi.org/10.1029/2018JD029667>

933 Goddard, J. W. F., Tan J., and Thurai M. , 1994: Technique for calibration of meteorological radar
934 using differential phase. *Electron. Lett.*, 30 , 166–167.

935 Gorgucci, E., R. Bechini, L. Baldini, R. Cremonini, and V. Chandrasekar, 2013: The Influence of
936 Antenna Radome on Weather Radar Calibration and Its Real-Time Assessment. *J. Atmos.*
937 *Oceanic Technol.*, 30, 676–689, <https://doi.org/10.1175/JTECH-D-12-00071.1>.

938 Dupont, J.C. M. A. Drouin, J.F. Ribaud, A. Gibe, J. Delanoe, F. Toledo, L. Pfitzenmaier, G.
939 Ghiggi, M. Schleiss: 2022 Hands-on training » on the monitoring of stability of DCR
940 reflectivity using disdrometers ACTRIS-CCRES workshop, November 14-15th 2022,
941 SIRTA Observatory.

942

943 Hardin, J., A. Hunzinger, E. Schuman, A. Matthews, N. Bharadwaj, A. Varble, K. Johnson, and
944 S. Giangrande, 2020: CACTI Radar b1 Processing: Corrections, Calibrations, and
945 Processing Report. Tech. Doc. DOE/SC-ARM-
946 TR244, 46 pp., <https://arm.gov/publications/brochures/doe-sc-arm-tr-244.pdf>.

947 Hardin, J., Giangrande, S. E., and Zhou, A. Laser Disdrometer Quantities (LDQUANTS) and
948 Video Disdrometer Quantities (VDISQUANTS) Value-Added Products Report. United
949 States: N. p., 2020. Web. doi:10.2172/1808573.

950 Hunzinger, A, JC Hardin, N Bharadwaj, A Varble, and A Matthews. 2020. “An Extended Radar
951 Relative Calibration Adjustment (eRCA) Technique for Higher Frequency Radars and RHI
952 Scans.” *Atmospheric Measurement Techniques Discussions*, [https://doi.org/10.5194/amt-](https://doi.org/10.5194/amt-2020-57)
953 [2020-57](https://doi.org/10.5194/amt-2020-57)

954 Jensen, M. P., D. Collins, P. Kollias, D. Rosenfeld, A. Varble, S. Collis, J. Fan, R. Griffin, R.
955 Jackson, T. Logan, G. McFarquhar, J. Quaas, R. Sheesley, P. Stier, S. van den Heever, Y.
956 Wang, G. Zhang, E. Bruning, A. Fridlind, C. Kuang, A. Ryzkhov, S. Brooks, . Defer, S.
957 E. Giangrande, J. Hu, M. Kumjian, T. Matsui, C. Nowotarski, M. Oue., J. Snyder, S.
958 Usenko, M. van Lier Walqui, and Y. Xu, 2019: TRacking Aerosol Convection Interactions
959 Experiment (TRACER) Science Plan. DOE/SC-ARM-19-017. 30 pp.

960 Jensen, M. P., L. Judd, P. Kollias, J. Sullivan, R. Nadkarni, C. Kuang, G. McFarquhar, H. Powers
961 and J. Flynn, 2022: A succession of cloud, precipitation, aerosol and air quality field

962 experiments in the coastal urban environment. *Bull. Amer. Meteor. Soc.*,
963 <https://doi.org/10.1175/BAMS-D-21-0104.1>.

964 Jensen, M. P., J. H. Flynn, P. Kollias, C. Kuang, G. McFarquhar, H. Powers, S. Brooks, E. Bruning,
965 D. Collins, S. M. Collis, J. Fan, A. Fridlind, S. E. Giangrande, R. Griffin, J. Hu, R. C.
966 Jackson, M. Kumjian, T. Logan, T. Matsui, C. Nowotarski, M. Oue, A. Rapp, D. Rosenfeld,
967 A. Ryzhkov, R. Sheesley, J. Snyder, P. Stier, S. Usenko, S. van den Heever, M. van Lier-
968 Walqui, A. Varble, Y. Wang, A. Aiken, M. Deng, D. Dexheimer, M. Dubey, Y. Feng, V.
969 Ghate, K. L. Johnson, K. Lamer, S. Saleeby, D. Wang, M. Zawadowicz and A. Zhou, 2023:
970 TRacking Aerosol Convection interactions ExpeRiment (TRACER) final campaign report.
971 DOE/SC-ARM-3-038. 132 pp.

972
973 Kollias, P., Bharadwaj N., Widener K. , Jo I. , and Johnson K. , 2014a: Scanning ARM cloud
974 radars. Part I: Operational sampling strategies. *J. Atmos. Oceanic Technology*, in press.

975 Kollias, P., and Coauthors, 2014b: Scanning ARM Cloud Radars. Part II: Data Quality Control
976 and Processing. *J. Atmos. Oceanic Technol.*, 31, 583–
977 598, <https://doi.org/10.1175/JTECH-D-13-00045.1>.

978 Kollias, P., E. E. Clothiaux, M. A. Miller, B. A. Albrecht, G. L. Stephens, and T. P. Ackerman,
979 2007: Millimeter-Wavelength Radars: New Frontier in Atmospheric Cloud and
980 Precipitation Research. *Bull. Amer. Meteor. Soc.*, 88, 1608–
981 1624, <https://doi.org/10.1175/BAMS-88-10-1608>.

982 Kollias, P., and Coauthors, 2020: The ARM Radar Network: At the Leading Edge of Cloud and
983 Precipitation Observations. *Bull. Amer. Meteor. Soc.*, 101, E588–
984 E607, <https://doi.org/10.1175/BAMS-D-18-0288.1>.

985 Kollias, P., B. P. Treserras, and A. Protat, 2019: Calibration of the 2007–2017 record of
986 Atmospheric Radiation Measurements cloud radar observations using CloudSat,
987 *Atmospheric Measurement Techniques*, 12, 4949–4964, [https://doi.org/10.5194/amt-12-](https://doi.org/10.5194/amt-12-4949-2019)
988 4949-2019

- 989 Kurri, M., and A. Huuskonen, 2008: Measurements of the transmission loss of a radome at
990 different rain intensities. *J. Atmos. Oceanic Technol.*, 25, 1590–1599.
- 991 Lamer, K., Mariko Oue, Alessandro Battaglia, Richard J. Roy, Ken B. Cooper, Ranvir
992 Dhillon, and Pavlos Kollias 2021: Multifrequency radar observations of clouds and
993 precipitation including the G-band. *Atmospheric Measurement Techniques*. Volume 14,
994 issue 5 *AMT*, 14, 3615–3629, 2021 <https://doi.org/10.5194/amt-14-3615-2021>
- 995 Lhermitte, R., 2002: *Centimeter and Millimeter Wavelength Radars in Meteorology*. Lhermitte
996 Publications, 550 pp.
- 997 Liu, Y. and Mace, G. G.: Assessing synergistic radar and radiometer capability in retrieving ice
998 cloud microphysics based on hybrid Bayesian algorithms, *Atmos. Meas. Tech.*, 15, 927–
999 944, <https://doi.org/10.5194/amt-15-927-2022>, 2022.
- 1000 Louf, V., A. Protat, R. A. Warren, S. M. Collis, D. B. Wolff, S. Raunyar, C. Jakob, and W. A.
1001 Petersen, 2019: An Integrated Approach to Weather Radar Calibration and Monitoring
1002 Using Ground Clutter and Satellite Comparisons. *J. Atmos. Oceanic Technol.*, 36, 17–
1003 39, <https://doi.org/10.1175/JTECH-D-18-0007.1>.
- 1004 Luca Baldini, V. Chandrasekar & Dmitri Moisseev (2012) Microwave radar signatures of
1005 precipitation from S band to Ka band: application to GPM mission, *European Journal of*
1006 *Remote Sensing*, 45:1, 75-88, DOI: 10.5721/EuJRS20124508
- 1007 Maahn, M., Hoffmann, F., Shupe, M. D., de Boer, G., Matrosov, S. Y., and Luke, E. P.: Can liquid
1008 cloud microphysical processes be used for vertically pointing cloud radar calibration?,
1009 *Atmos. Meas. Tech.*, 12, 3151–3171, <https://doi.org/10.5194/amt-12-3151-2019>, 2019.
- 1010 Matrosov, S. Y., 2005: Attenuation-Based Estimates of Rainfall Rates Aloft with Vertically
1011 Pointing Ka-Band Radars. *J. Atmos. Oceanic Technol.*, 22, 43–
1012 54, <https://doi.org/10.1175/JTECH-1677.1>.

1013 Matthews, A., M. Deng, E. Schuman, Y.Feng, M. Rocque, 2024: SAIL Radar B1 Processing:
1014 Corrections, Calibrations, and Processing Report. U.S. Department of Energy,
1015 Atmospheric Radiation Measurement user facility, Richland, Washington. In preparation.

1016 Mead, J. 2010. MMCR Calibration Study. U.S. Department of Energy. DOE/SC-ARM/TR-088.

1017 Meagher, Jonathan P., and Ziad S. Haddad. “To What Extent Can Raindrop Size Be Determined
1018 by a Multiple-Frequency Radar?” *Journal of Applied Meteorology and Climatology*, vol.
1019 45, no. 4, 2006, pp. 529–36. JSTOR, <http://www.jstor.org/stable/26171702>. Accessed 13
1020 Mar. 2023.

1021 Miller, M. A., K. Nitschke, T. P. Ackerman, W. R. Ferrell, N. Hickmon, and M. Ivey, 2016: The
1022 ARM Mobile Facilities. *Meteor. Monogr.*, 57, 9.1–
1023 9.15, <https://doi.org/10.1175/AMSMONOGRAPHS-D-15-0051.1>.

1024 Muradyan, P, and Coulter, R.: Radar Wind Profiler (RWP) and Radio Acoustic Sounding System
1025 (RASS) instrument handbook, U. S. Department of Energy, Atmospheric Radiation
1026 Measurement user facility, DOE/SC-ARM-TR-044, <https://doi.org/10.2172/1020560>,
1027 2020.

1028 Myagkov, A., Kneifel, S., and Rose, T.: Evaluation of the reflectivity calibration of W-band radars
1029 based on observations in rain, *Atmos. Tech.*, 13, 5799–5825, [https://doi.org/10.5194/amt-](https://doi.org/10.5194/amt-13-5799-2020)
1030 [13-5799-2020](https://doi.org/10.5194/amt-13-5799-2020), 2020.

1031 Protat, A., D. Bouniol, E. J. O’Connor, H. Klein Baltink, J. Verlinde, and K. Widener, 2011:
1032 CloudSat as a Global Radar Calibrator. *J. Atmos. Oceanic Technol.*, 28, 445–452,
1033 <https://doi.org/10.1175/2010JTECHA1443.1>.

1034 Rocque, M. M. Deng, Y.Feng, E. Schuman, I. Silber, A. Matthews, T. Wendler, V. Castro, Iosif
1035 Lindenmaier, 2024: EPCAPE Radar b1 Processing: Corrections, Calibrations, and
1036 Processing Report, U.S. Department of Energy, Atmospheric Radiation Measurement user
1037 facility, Richland, Washington. In preparation.

1038 Ryzhkov, AV, SE Giangrande, VM Melnikov, and TJ Schuur. 2005. "Calibration Issues of Dual-
1039 Polarization Radar Measurements." *Journal of Atmospheric and Oceanic Technology*
1040 22(8): 1138– 1155, <https://doi.org/10.1175/JTECH1772.1>

1041 Segelstein, D. J., "The complex refractive index of water," University of Missouri-Kansas City,
1042 (1981).

1043 Thompson, R., A. Illingworth, T. Darlington, and J. Ovens, 2012: Correcting attenuation in
1044 operational radars from both heavy rain and the radome using the observed microwave
1045 emission. *Proc. Seventh European Conf. on Radar in Meteorology and Hydrology*,
1046 Toulouse, France, ERAD, 8A.5.

1047 Tridon, F., Battaglia, A., Kollias, P., Luke, E., and Williams, C. R.: Signal postprocessing and
1048 reflectivity calibration of the Atmospheric Radiation Measurement Program 915-MHz
1049 Wind Profilers, *J. Atmos. Ocean. Tech.*, 30, 1038-1054. <https://doi.org/10.1175/JTECH->
1050 [D-12-00146.1](https://doi.org/10.1175/JTECH-D-12-00146.1), 2013.

1051 Ulaby, F. T., R.K. Moore, and A.K. Fung, 1981: *Microwave Remote Sensing. Vol. 1*, Addison-
1052 Wesley, 456pp.

1053 Varble, A. C., and Coauthors, 2021: Utilizing a Storm-Generating Hotspot to Study Convective
1054 Cloud Transitions: The CACTI Experiment. *Bull. Amer. Meteor. Soc.*, 102, E1597–
1055 E1620, <https://doi.org/10.1175/BAMS-D-20-0030.1>.

1056 Wang D, S Giangrande, M Bartholomew, J Hardin, Z Feng, R Thalman, and L Machado.
1057 2018. "The Green Ocean: precipitation insights from the GoAmazon2014/5
1058 experiment." *Atmospheric Chemistry and Physics*, 18(12), 10.5194/acp-18-9121-2018.

1059 Wang D, S Giangrande, Bartholomew, J Hardin 2021: Analysis of Three Types of Collocated
1060 Disdrometer Measurements at the ARM Southern Great Plains Observatory, DOE/SC-
1061 ARM-TR-275. <https://www.arm.gov/publications/programdocs/doe-sc-arm-tr-275.pdf>

1062 Widener, K. B. and J. B Mead 2004: *W-Band ARM Cloud Radar – Specifications and Design*

1063 Fourteenth ARM Science Team Meeting Proceedings, Albuquerque, New Mexico, March 22-26,

1064 Widener, K., N Bharadwaj, and K. Johnson, 2012: Ka-Band ARM Zenith Radar (KAZR)

1065 handbook. DOE/SC-ARM/TR-106

1066 https://www.arm.gov/publications/tech_reports/handbooks/kazr_handbook.pdf

1067 Wolff, DB, DA Marks, and WA Petersen. 2015. "General Application of the Relative Calibration

1068 Adjustment (RCA) Technique for Monitoring and Correcting Radar Reflectivity

1069 Calibration." *Journal of Atmospheric and Oceanic Technology* 32(3): 496–506,

1070 <https://doi.org/10.1175/JTECH-D-13-00185.1>

1071 Williams, C. R., Gage, K. S., Clark, W., and Kucera, P.: Monitoring the reflectivity calibration of

1072 a scanning radar using a profiling radar and a disdrometer, *J. Atmos. Oceanic Technol.*, 22,

1073 1004-1018, 2005.

1074 Williams, C.R., Barrio, J., Johnston, J. E., Myradyan, P. and Giangrande, S. E.: Calibrating radar

1075 wind profiler reflectivity factor using surface disdrometer observations, *J. Atmos. Meas.*

1076 *Techn.*, in review, <https://egusphere.copernicus.org/preprints/2023/egusphere-2022-1405>,

1077 2023.

1078 Xingjian Yu, Yu Zhang, Run Hu, Xiaobing Luo, 2021: Water droplet bouncing dynamics, *Nano*

1079 *Energy*, Volume 81, 2021, 105647, ISSN 2211-

1080 2855, <https://doi.org/10.1016/j.nanoen.2020.105647>.

1081 Zhang, G., J. Vivekanandan and E. Brandes, "A method for estimating rain rate and drop size

1082 distribution from polarimetric radar measurements," in *IEEE Transactions on Geoscience*

1083 *and Remote Sensing*, vol. 39, no. 4, pp. 830-841, April 2001, doi: 10.1109/36.917906.

1084 Zhu, Z., Lamer, K., Kollias, P., & Clothiaux, E. E. (2019). The vertical structure of liquid water

1085 content in shallow clouds as retrieved from dual-wavelength radar observations. *Journal of*

1086 *Geophysical Research:*

1087 *Atmospheres*, 2019; 124: 14184– 14197. <https://doi.org/10.1029/2019JD031188>

1088